# Influence of particulate versus diffusive molybdenum supply mechanisms on the molybdenum isotope composition of continental margin sediments

Sümeyya Eroglu, Florian Scholz, Martin Frank, Christopher Siebert

GEOMAR Helmholtz Centre for Ocean Research Kiel, Wischhofstraße 1-3, 24148 Kiel

## Abstract

The sedimentary concentration and stable isotope composition of molybdenum (Mo) is widely used as a proxy for paleo redox conditions in the marine environment. However, the behavior of Mo during early diagenesis is still not fully understood, which complicates the application of the Mo proxy in ancient continental margin environments. Here, we present Mo concentrations and isotope compositions of sediment and pore water samples from the Guaymas Basin in the Gulf of California. Our sample set covers a broad range of depositional environments, including sediments from within the eastern equatorial Pacific oxygen minimum zone (OMZ), from a semi-restricted oxic graben, and from near a hydrothermal vent-field. By investigating Mo cycling in these different settings, we provide new insights into different modes of Mo fixation and the associated isotope fractionation.

Sediments from the OMZ have authigenic Mo concentrations ($Mo_{auth}$) between 3.3 and 17.2 µg/g and $\delta^{98}Mo$ between +1.64 and +2.13 ‰. A linear decrease in pore water Mo concentrations to the depth were hydrogen sulfide accumulates along with sedimentary authigenic $\delta^{98}Mo$ values ($\delta^{98}Mo_{auth}$) close to seawater indicate diffusion of Mo from the bottom water into the sediment with little isotope fractionation during quantitative Mo removal. Sediments from the site with oxic bottom water within the basin reveal $Mo_{auth}$ concentrations ranging from 1.2 to 14.7 µg/g and $\delta^{98}Mo_{auth}$ signatures between -1.39 to +2.07 ‰. Pore water Mo concentrations are generally higher than ambient bottom water concentrations and the light $\delta^{98}Mo_{auth}$ signatures of the pore waters between +0.50 and +0.80 ‰ and of the sediments indicate continuous Mo exchange between the pore water Mo pool and Mn and Fe oxides during early diagenesis. Sediment samples from the vent field mainly consist of black smoker debris and are characterized by $Mo_{auth}$ concentrations ranging from 8.6 to 33.2 µg/g and $\delta^{98}Mo_{auth}$ values as high as +2.20 ‰. The relatively high Mo concentrations and seawater-like $\delta^{98}Mo$ can be explained by near-quantitative Mo scavenging from hydrothermal solutions with little isotope fractionation at high

temperatures. Comparison of our new data for the OMZ sediments in the Gulf of California with previously published data for sediments from the Peruvian OMZ highlights that Mo isotope compositions in this kind of setting strongly depend on how Mo is delivered to the sediment. If Mo delivery into the sediment contributes to Mo accumulation in the solid phase, as is the case in the Guaymas Basin, sedimentary $Mo_{auth}$ concentrations are relatively low but the isotope values are close to the $\delta^{98}Mo$ signal of seawater. If Mo is exclusively delivered by particles, like on the Peruvian margin, much higher sedimentary $Mo_{auth}$ concentrations can be attained. In the latter case, $Mo_{auth}$ isotope values will be lighter because the sediments preserve the isotopic offset that was generated during adsorption or uptake of Mo by particles. Our findings de-emphasize the role of dissolved Mo speciation in pore waters but highlight the importance of the mode of Mo delivery for the Mo concentration and isotope composition preserved in the paleo-record.

Keywords: Molybdenum (Mo), Early Diagenesis, Paleo-redox, Oxygen minimum zone, Hydrothermal vent

## 1. Introduction

The Mo concentration and isotope composition of marine sediments is a widely used proxy for the reconstruction of redox conditions in modern and paleo environments (Crusius et al., 1996; Siebert et al., 2003; e.g. Arnold et al., 2004; Barling and Anbar, 2004; Poulson et al., 2006; Poulson-Brucker et al., 2009). This is due to the changing geochemical behavior of Mo under different redox conditions. In an oxygenated water column, dissolved Mo in seawater and pore waters has a high affinity for Mn and Fe oxides, which preferentially adsorb light Mo isotopes (Siebert et al., 2003; Barling and Anbar, 2004; Tossell, 2005; McManus et al., 2006; Goldberg et al., 2009) (Fig. 1). The isotopically light "oxic sink" covers about 35 % of the global sedimentary Mo budget (Scott et al., 2008), causing a shift in the isotopic signature of the seawater Mo pool to a $\delta^{98}Mo$ value of about +2.34 ‰ (Barling et al., 2001; Siebert et al., 2003; Nakagawa et al., 2012). In contrast, when dissolved hydrogen sulfide ($H_2S$) is present in the water column and exceeds a value of 11 µM (Erickson and Helz, 2000), Mo is effectively scavenged from seawater into the sediment. Such settings are described as "euxinic" and $\delta^{98}Mo$ of these sediments

57 can reach isotopically heavy compositions close to open-ocean seawater values (Fig. 1). However,
58 permanent $H_2S$ availability in the water column is limited to restricted basins, e.g. the Black Sea and the
59 Cariaco Trench (e.g. Emerson and Huested, 1991). Thus, euxinic settings only cover about 15 % of the
60 sedimentary Mo budget (Scott et al., 2008). Nevertheless, most studies applying the Mo redox proxy are
61 based on the geochemical mechanisms under permanently euxinic conditions (Helz et al., 1996; e.g.
62 Erickson and Helz, 2000; Nägler et al., 2011), although this only represents a small fraction of Mo fixed
63 in the marine environment. Indeed, the probably largest Mo sink (~ 50 %) are sediments of open marine
64 continental margins (McManus et al., 2006). These sediments are governed by a wide spectrum of redox
65 conditions during early diagenesis. Early diagenesis is driven by the settling and remineralization of
66 organic matter in the sediment (Froelich et al., 1979), where oxidants serve as electron acceptors
67 depending on their availability according to the decreasing free energy yield of the corresponding
68 pathway (oxic respiration > nitrate reduction > Mn oxide reduction > Fe oxide reduction > sulfate
69 reduction) (Froelich et al., 1979; Burdige, 1993; Canfield and Thamdrup, 2009). As a consequence of
70 the consecutive usage of electron acceptors with changing sedimentary conditions, different chemical
71 zones can be observed in the sediment which are named oxic, nitrogenous, manganous, ferruginous and
72 sulfidic. Most of the processes taking place in these zones are known to be accompanied by Mo isotope
73 fractionation (see Section 2 for more details). Consequently, early diagenesis can result in a wide range
74 of Mo isotope compositions (Fig. 1), which often overlap and are thus difficult to assign to specific
75 environmental conditions or processes.
76 In upwelling areas along continental margins with high rates of primary production oxygen utilization
77 by organic matter remineralization can lead to low or zero oxygen concentrations in the water column,
78 so-called oxygen minimum zones (OMZ) (Pennington et al., 2006; Ulloa et al., 2012; e.g. Kalvelage et
79 al., 2013). In OMZs, denitrification (Lam et al., 2009a; Zehr, 2009; Dalsgaard et al., 2012) and reduction
80 of Mn oxides (Boning et al., 2004; Scholz et al., 2011; Hawco et al., 2016; Scholz et al., 2017) already
81 occur in the water column. Furthermore, OMZ sediments can release dissolved ferrous iron (Fe(II))
82 (Noffke et al., 2012; Scholz et al., 2014; Chever et al., 2015) and occasionally dissolved hydrogen sulfide
83 ($H_2S$) to the water column (Schunck et al., 2013; Scholz et al., 2016; Sommer et al., 2016). Sediments
84 in these settings also show variable $\delta^{98}$Mo signatures and an average $\delta^{98}$Mo value of ~1.6 ‰ has been

proposed to represent "anoxic open ocean" settings, where $H_2S$ is mainly restricted to the pore water (Poulson et al., 2006; Siebert et al., 2006; Poulson-Brucker et al., 2009). Considering the importance of open marine continental margins for the global Mo budget, the understanding of these settings is fundamental and has important implications for the interpretation of the paleo-record. Yet, the mechanisms of Mo removal and fixation in these environments are still not fully understood.

In this study, we investigate Mo cycling in distinct redox settings of the Guaymas Basin in the Gulf of California (Mexico). Sediments were sampled on the continental slope within the eastern equatorial Pacific OMZ and in the oxic part of the basin. In addition, samples were taken near a hydrothermal vent field, where sediments mainly consist of vent debris. Hydrothermal vent deposits are highly enriched in a wide range of metals, including Mo, (e.g. Trefry et al., 1994; Metz and Trefry, 2000) and can give additional insights into early diagenetic processing of Mo originating from interaction between seawater and a hydrothermal vent. Solid phase and pore water samples were analyzed for selected geochemical parameters, as well as their Mo concentration and isotope composition. The main goal of this study is to gain insights into Mo fractionation effects during early diagenesis under different boundary conditions and to improve interpretations of paleo-redox records in open-marine settings.

## 2. Molybdenum isotope fractionation and speciation in the marine environment

The main Mo source to the ocean is from the continental crust, which has an average $\delta^{98}$Mo isotope composition of +0.2 ‰ (Willbold and Elliott, 2017) (Fig. 1). The main transport pathway of Mo from the continent to the ocean are rivers (Morford and Emerson, 1999; McManus et al., 2006), which show an average $\delta^{98}$Mo value of +0.7 ‰ (Archer and Vance, 2008) (Fig. 1). In oxic seawater, Mo behaves conservatively as oxymolybdate ($Mo(VI)O_4^{2-}$), shows homogenous concentrations of ~110 nM at a salinity of 35, and has a long residence time of ~440 ka (Collier, 1985; Emerson and Huested, 1991; Miller et al., 2011). The Mo isotope fractionation processes that define the oceanic Mo isotope reservoirs are governed by changes in the Mo speciation under different redox conditions. As outlined above, the high affinity of light Mo isotopes in particular towards Mn oxides leaves the seawater isotopically heavy with respect to the continental input. The equilibrium fractionation laws outlined by Bigeleisen and Mayer (1947) and Urey (1947) would predict a heavy isotope composition in the solid phase (i.e. Mn

oxides) when compared to the contemporaneous aqueous phase (i.e. seawater). However, the light isotope fractionation is induced by a change in coordination during adsorption. In detail, particulate Mn oxides in the oxic water column and sediment very effectively adsorb tetrahedrally coordinated oxymolybdate from the ambient solution on their reactive surfaces (Bertine and Turekian, 1973; Calvert and Pedersen, 1993; Zheng et al., 2000; Kashiwabara et al., 2011). During this process the coordination state is changed from tetrahedral to octahedral (Kashiwabara et al., 2011) resulting in an isotopic fractionation for $\Delta^{98}Mo_{solution\text{-}Mn\text{-}oxides}$ of +2.7 to +3.2 ‰ (Siebert et al., 2003; Barling and Anbar, 2004; Tossell, 2005; McManus et al., 2006). The structural change of the Mo species adsorbed from seawater to Fe-oxides and therefore associated Mo isotope fractionation is smaller and more variable ($\Delta^{98}Mo_{solution\text{-}Fe\text{-}oxides}$ of +0.83 to +2.19 ‰) depending on the mineralogy and crystallinity of the Fe oxide minerals (Goldberg et al., 2009; Kashiwabara et al., 2011). Experimental fractionation factors increase from magnetite ($\Delta^{98}Mo$ = +0.83 ‰) to ferrihydrite ($\Delta^{98}Mo$ = +1.11 ‰) to goethite ($\Delta^{98}Mo$ = +1.39 ‰) to hematite ($\Delta^{98}Mo$ = +2.19 ‰) (Goldberg et al., 2009). Under anoxic-sulfidic conditions aqueous hydrogen sulfide ($H_2S$; $\Sigma S^{2-} = H_2S + HS^- + S^{2-}$) is present in the water column or in pore waters and oxymolybdate is transformed to tetra-thiomolybdate ($Mo(VI)S_4^{2-}$) with increasing $H_2S$, following a series of intermediate steps of oxy-thiomolybdate formation ($Mo(VI)O_{4-x}S_x^{2-}; x = 1, 2, 3, 4$) (Helz et al., 1996; Erickson and Helz, 2000; Vorlicek and Helz, 2002; Dahl et al., 2013). This transformation involves an isotopic fractionation associated with each sulfidation step (Tossell, 2005; Dahl et al., 2010; Nägler et al., 2011). Above a threshold value of 11 µM $H_2S$ the transition from oxy-molybdate to thio-molybdate is highly effective and Mo is quantitatively scavenged into sulfidic sediments (Erickson and Helz, 2000). Thiomolybdate is particle reactive and readily scavenged from the water column by protonated particle surfaces, either by the irreversible incorporation into Fe-Mo-sulfides (Helz et al., 1996; Helz et al., 2014) or the adsorption onto sulfurized organic matter (Helz et al., 1996; Tribovillard et al., 2004; Chappaz et al., 2014; Dahl et al., 2017; Wagner et al., 2017), thereby retaining Mo in the sediment (Raiswell and Plant, 1980; Huerta-Diaz and Morse, 1992; Dellwig et al., 2002; Bostick et al., 2003).

## 3. Study area and description of sampling sites

141 The Gulf of California is located in the Eastern Equatorial Pacific between Baja California and the
142 Mexican mainland (Fig. 2). During late fall and early spring strong northwesterly winds transport surface
143 water out of the Gulf, induce upwelling of nutrient-rich North Pacific Intermediate Water (NPIW), and
144 high rates of primary production (Thunell et al., 1993; Thunell et al., 1994; Thunell, 1998). In summer
145 the winds reverse to weak southeasterlies resulting in the in-flow of tropical surface water and
146 subtropical subsurface water into the Gulf, which causes a decline of upwelling and primary production
147 and higher terrigenous fluxes (Thunell et al., 1993). The average primary production is ~130 g C $m^{-2}$
148 $yr^{-1}$ (Brumsack, 1989) and consists of biogenic silica (~ 64 %), carbonate (~ 19%), and organic carbon
149 (~ 7%) (Thunell, 1998). The upwelling water masses are oxygen depleted and further oxygen is
150 consumed by respiration of exported organic material. Consequently, the Gulf of California is
151 characterized by an OMZ (< 2 µM $O_2$) between about 500 and 1000 m water depth (Wyrtki, 1962; Bray,
152 1988; Thunell, 1998).
153 The Gulf of California is part of the East Pacific Rise spreading regime. Early continental rifting in the
154 Guaymas basin within the central Gulf of California (Fig. 2a) has led to the formation of graben
155 structures and of hydrothermal vent fields (Moore, 1973; e.g. Gieskes et al., 1982; von Damm et al.,
156 1985). Due to high sedimentation rates in the Guaymas basin of up to 3.5 m $kyr^{-1}$ (Donegan and
157 Schrader, 1982), the hydrothermal vent fields are hosted by several hundred meter thick organic-rich
158 hemipelagic sediments (Calvert, 1966; von Damm et al., 1985; Berndt et al., 2016).
159 The subject of this study are sediments from the Guaymas Basin, which is up to 2200 m deep, 240 km
160 long and 60 km wide. Sediment fluxes within the Guaymas Basin are dominated by biogenic silica
161 during the productive winter season and lithogenic material during the rainy summer season (Calvert,
162 1966; Brumsack, 1989; Thunell, 1998). Sedimentation rates in the Guaymas Basin range from 0.4 to 3.5
163 m $kyr^{-1}$ (Donegan and Schrader, 1982). We investigate short sediment cores (< 40 cm depth) from three
164 sites (Fig. 2 a-c; Table 1 in data repository), which were retrieved during *R.V. Sonne* cruise SO241 using
165 a multiple corer device (MUC) (Table 1 in data repository). Core MUC9 was retrieved on the slope at
166 667 m water depth, where anoxic conditions in the bottom water prevail (Fig. 2b). Sediments within the
167 OMZ are laminated (Calvert, 1966) as a consequence of the general absence of bioturbating bottom-
168 fauna under oxygen-deficient conditions. Laminae reflect the seasonally changing input of mainly

lithogenic or siliceous material. Average total organic carbon (TOC) concentrations are 3.32 ± 0.35 wt-% (2SD). Core MUC3 was retrieved in the deep basin within a spreading-related graben at 2043 m water depth. MUC9 and MUC3 consist of hemipelagic sediment, i.e. fine-grained clay and silt with variable contributions of lithogenic and siliceous material from continental sources and from diatoms. At this graben site, weakly oxic conditions (~37 µM $O_2$) prevail in the bottom water (Fig. 2c). Average TOC concentration are slightly lower than in the OMZ core reaching 2.89 ± 0.98 wt-% (2SD). Core MUC16 was retrieved at 1853 m water depth (Fig. 2c) within a recently discovered hydrothermal vent field (Berndt et al., 2016). The core consists of black smoker chimney debris and is heterogeneously mixed with hemipelagic sediment. It shows the lowest TOC concentrations of the three sites (1.69 ± 1.18 wt-%, 2SD) and the bottom waters are weakly oxic (~25 µM). The three cores will be referred to as 'OMZ core', 'graben core' and 'vent-related core' in the following.

## 4. Methods

### 4.1. Sample preparation and element concentration measurements

Sediment and pore water sampling was performed following descriptions by Scholz et al. (2011). MUCs were plugged after recovery and further handled in a cooled lab at approximate seafloor temperature. After bottom water had been removed with a plastic tube, the sediment core was subsampled in an argon-filled glove bag. Sediment cores were cut into 1-4 cm slices, which were centrifuged to extract the pore water. The supernatant was filtered through cellulose acetate membrane filters with 0.2 µm pore size in a second argon-filled glove bag.

An aliquot of filtered pore water was acidified using distilled concentrated $HNO_3$ and stored in acid-cleaned HDPE vials. Ferrous Fe and $H_2S$ concentrations in pore water were determined on unacidified samples after filtration by standard spectrophotometric techniques (Cline, 1969; Stookey, 1970). Molybdenum concentrations of bottom and pore waters were measured by isotope dilution using an enriched $^{95}Mo$ spike. Analyses of Mo and Mn concentrations were conducted on an inductively coupled plasma mass spectrometer (ICP-MS) at GEOMAR in Kiel and reproducibility of repeated analyses was <4% 1 sigma relative standard deviation (RSD). External reproducibility of repeated measurements (n = 7) of the seawater samples CASS-5 (Nearshore Seawater; Canadian Research Council) and

197 NASS-6 (Seawater; Canadian Research Council) was better than 5% (RSD). The measured Mo
198 concentration was 99.3 ± 2.7 nM (certified value 102.1 nM) for CASS-5 and 102.8 ± 4.0 nM (certified
199 value 103.1 nM) for NASS-6.
200 Sediment samples were freeze-dried, powdered with an agate mill, and weighed into PFE vials. Total
201 organic carbon (TOC) and total sulfur (TS) analyses of sediment samples were determined by flash
202 combustion in a Carlo-Erba Element Analyzer (NA1500) and analytical precision for replicate analyses
203 was about 1% (RSD). About 100 mg of sediment per sample was digested in a HF-$HNO_3$-$HClO_4$ acid
204 mixture, and placed on a hotplate at 185°C over night. Digested samples were subsequently evaporated,
205 re-dissolved in concentrated $HNO_3$, placed on a hotplate at 130°C for 24 hours, again evaporated and
206 finally re-dissolved in diluted $HNO_3$. Major and trace element concentrations of dissolved sediment
207 samples were determined via inductively coupled plasma optical emission spectrometry (ICP-OES,
208 Varian 720-ES) and mass spectrometry (ICP-MS, Agilent Technologies 7500 Series) analyses. External
209 reproducibility of reference standards SDO-1 (Devonian Ohio Shale, USGS), MESS-3 (Marine
210 Sediment Reference Material, Canadian Research Council), PACS-3 (Marine Sediment Reference
211 Material, Canadian Research Council), and BHVO-1 (Basalt, Hawaiian Volcanic Observatory, USGS)
212 was <1% (RSD) for Al, Mn, and Fe and <5% (RSD) for Mo. Molybdenum concentrations are reported
213 as authigenic Mo ($Mo_{auth}$), which excludes the lithogenic Mo fraction, calculated from the Al
214 concentration and the Mo/Al ratio (Mo is given in ppm, Al in wt-%) of the lithogenic background
215 ($(Mo/Al)_{UCC}$ of 0.13 x $10^{-4}$, upper continental crust (UCC), Rudnick and Gao (2003)):

216 $$Mo_{auth} = Mo_{total} - (Mo/Al)_{UCC} * Al_{total}$$

217

218 4.2. Iron speciation

219 A sequential extraction for the recovery of highly reactive Fe phases (Poulton and Canfield, 2005) was
220 applied to the freeze-dried and ground sediment samples (see Scholz et al. (2019) for details). In brief,
221 1) Na acetate extracts Fe-carbonate and –monosulfide, 2) A hydroxylamine-HCl mixture extracts
222 low-crystalline Fe oxides, 3) Dithionite extracts high-crystalline Fe oxides, 4) Oxalate extracts
223 magnetite, and 5) Chromous chloride distillation extracts pyrite Fe ($Fe_{Py}$). In the following, the first four
224 fractions are summarized as unpyritized reactive Fe ($Fe_R$). The sum of $Fe_R$ and $Fe_{Py}$ is referred to as

highly reactive Fe ($Fe_{HR}$). $Fe_{Py}/Fe_{HR}$ ratios are given in the data repository ($Fe_{Py}$ and $Fe_{HR}$ concentrations are given in wt-%). Any remaining Fe fraction represents unreactive silicate Fe.

4.3. Molybdenum isotope analyses

The Mo purification procedure is based on the protocols of Siebert et al. (2001), Voegelin et al. (2009) and Wille et al. (2007). Prior to chemical separation, we added an adequate amount of $^{100}Mo$-$^{97}Mo$ double spike to the sediment and pore water samples in order to correct for any isotope fractionation during laboratory treatment and instrumental mass bias. Molybdenum was separated from the matrix and mass-interfering elements via ion exchange column chemistry using a column filled with 2 ml Biorad AG50W-X8 cation resin and washing and eluting with 0.5 M HCl, followed by a column filled with 1 ml Biorad AG1-X8 anion resin, washing with 4 M HCl and eluting with 2 M $HNO_3$. Yields after column chemistry were typically >90 % and procedural blanks were < 2 ng Mo which contributes less than 1% of total Mo.

Isotope analyses were carried out on a Nu Plasma MC-ICP-MS at the Isotope Geochemistry Labs at GEOMAR. Samples were introduced to the plasma ion source via a DSN-100 desolvating nebulizer system with an uptake rate of ~70 µl/min. Solutions had concentrations between 40 to 50 ng/ml and were measured at a signal of about 700 mV on $^{96}Mo$ using $10^{11}$ Ω resistors. We measured sediment samples in 4 blocks of 10 cycles per sample with a 10 s signal integration time each. Solutions of pore water samples had concentrations of around 30 ng/ml and were measured in 3 blocks of 10 cycles per sample with a 10 s signal integration time. Molybdenum concentrations in pore water are significantly lower (few to several tens of ng/g) than in the sediment and while the total recovery of pore water samples can be several ml in the upper few cm of the core, it often did not exceed 2 ml further downcore, depending on the porosity. Tests with diluted seawater reference materials ($\delta^{98}Mo$ of CASS-5: 2.04 ± 0.17 ‰ (n=5), NASS-6: 2.06 ± 0.10 ‰ (n=5), IAPSO: 2.05 ± 0.10 ‰ (n=5)) showed that the reproducibility of measurement solutions below 20 ng/ml exceeded the 2SD of the respective reference material. Thus, we only analyzed pore water samples that allowed measurements at 30 ng/ml and decreased the measurement cycles to 30 without compromising the reproducibility or measurement statistics.

Samples were measured relative to the Alfa Aesar Mo standard solution, Specpure #38791 (lot no. 011895D), which allowed a long-term external reproducibility of ± 0.07 ‰ (2SD, n = 201). The international standard NIST-SRM-3134 was also measured repeatedly during each measurement session and is offset from the Alfa Aesar standard by +0.15 ± 0.08 ‰ (2SD, n = 46), which is in agreement with published values of Greber et al. (2012) and Nägler et al. (2014). Following Nägler et al. (2014), we present the results in the δ-notation relative to NIST-SRM-3134 with an offset of +0.25 ‰ and expressed in permil [‰]:

$$\delta^{98}Mo\ [‰] = \left[\frac{{}^{98}Mo/{}^{95}Mo_{sample}}{{}^{98}Mo/{}^{95}Mo_{NIST-SRM-3134}} - 1\right] \times 1000 + 0.25$$

In order to determine a realistic long term reproducibility of a matrix sample, USGS rock reference material SDO-1 (Devonian Ohio Shale) was chemically processed and analyzed with each batch of samples. The external reproducibility is +1.03 ± 0.09 ‰ (2SD, n = 43), which is in agreement with values of Goldberg et al. (2013) and references therein.

Reported authigenic $\delta^{98}$Mo data ($\delta^{98}Mo_{auth}$) are calculated from the authigenic fraction ($Mo_{auth}$), assuming that the lithogenic Mo fraction has an average isotope composition of +0.2 ‰ ($\delta^{98}Mo_{UCC}$) (Willbold and Elliott, 2017):

$$\delta^{98}Mo_{auth} = \frac{\delta^{98}Mo_{total} - \left(\left(1 - \frac{Mo_{auth}}{Mo_{total}}\right) \times (\delta^{98}Mo_{UCC})\right)}{\frac{Mo_{auth}}{Mo_{total}}}$$

## 5. Results

### 5.1. Sediment and pore water concentrations of manganese, iron and sulfur

In all analyzed samples of the OMZ core, pore water concentrations of Mn are below 2 µM and corresponding Mn/Al ratios of the sediment are ~0.005 (Mn and Al ratios are given in wt-%) (Fig. 3a, Table 2, data repository), which is depleted relative to the upper continental crust (0.01, UCC, Rudnick and Gao (2003)). In contrast, sediments of the weakly oxic graben core are characterized by elevated Mn/Al relative to UCC (from 0.02 to 0.96 maximum at the top) and pore water Mn concentrations range from 160 to 291 µM with the highest value at 7 cm core depth (Fig. 3b, Table 3, data repository). The pore waters of the vent-related core also reveal elevated Mn concentrations similar to the graben core of

279 up to 79 µM in the uppermost cm and decrease down core to about 12 µM. Mn/Al ratios of the sediment
280 range from 0.025 to 0.143 (Fig. 3c, Table 4, data repository) and are thus slightly enriched relative to
281 the UCC value.
282 In the OMZ core aqueous Fe concentrations increase from values <0.5 µM in the bottom water to 62 µM
283 at 7 cm depth. Below this depth, aqueous Fe concentrations decrease again to values below 0.5 µM at
284 22 cm depth (Fig. 3a), where aqueous $H_2S$ accumulates in the pore water, indicating that Fe is removed
285 by reaction with sulfide. This is confirmed by the extent of pyritization ($Fe_{Py}/Fe_{HR}$), which increases
286 below this transition from ferruginous to sulfidic conditions in the pore water (Fig. 3a). In the graben
287 core pore water Fe concentrations increase from values <0.5 µM between 0 and 5 cm depth to 10 µM at
288 the bottom (Fig. 3b; Table 3, data repository). $Fe_{Py}/Fe_{HR}$ ratios increase at depths below 12 cm,
289 coincident with decreasing aqueous Fe concentrations (Fig. 3b). Pore water samples of the vent-related
290 core show the highest Fe concentrations of all three cores (up to 192 µM; Fig. 3c, Table 4, data
291 repository). $Fe_{Py}/Fe_{HR}$ ratios do not show a systematic depth trend and Fe concentrations are up to one
292 order of magnitude higher than concentrations within the OMZ and graben cores (Fig. 3a,b).
293
294 5.2. Molybdenum concentration and isotope composition of the solid phase and the pore waters
295 Bottom waters of all investigated sites show aqueous Mo concentrations (Tables 2-4, data repository)
296 that are indistinguishable from average seawater concentrations (~110 nM, Collier, 1985). In the OMZ
297 core Mo concentrations of the pore water reach 130 nM in the uppermost cm and then linearly decrease
298 to values of 5 nM at 26.5 cm sediment depth, where $H_2S$ accumulated (Fig. 3a, Table 2, data repository).
299 The graben core and the vent-related core are characterized by pronounced pore water Mo peaks in the
300 uppermost 5 cm with maximum values of 282 and 241 nM, respectively (Fig. 3 b,c, Tables 3 and 4, data
301 repository). These values are significantly higher than the average seawater concentration, which
302 indicates a Mo source other than seawater. Below these maxima, Mo removal from pore water is
303 reflected by decreasing concentrations to values of 47 nM and 57 nM at 30 and 13 cm depth, respectively
304 (Fig. 3 b,c).
305 $Mo_{auth}$ concentrations of the OMZ core sediment samples are relatively uniform and range from 3.27 to
306 8.54 µg $g^{-1}$, with one outlier at 13 cm depth (Fig. 3a). In the graben core, $Mo_{auth}$ concentrations show a

decreasing trend and reach a minimum of 1.23 µg $g^{-1}$ within the uppermost 6 cm. Below this depth, concentrations increase up to a maximum of 14.73 µg $g^{-1}$ at 30 cm depth (Fig. 3b). In the vent-related core, $Mo_{auth}$ concentrations overall increase from 8.9 to 33.2 µg $g^{-1}$ with depth (Fig. 3 c). These concentration changes indicate different processes governing the Mo geochemistry depending on the depositional conditions.

In the OMZ core, the $\delta^{98}Mo_{auth}$ of the sediments ranges from +1.64 to +2.13 ‰ (Fig. 3a). An isotopic shift is observed at the depth where pyritization increases. Above this depth, the average $\delta^{98}Mo_{auth}$ of the solid phase is +2.05 ± 0.11 ‰, whereas below it is +1.77 ± 0.20 ‰ (Fig. 3a). Measured pore water samples range from +0.74 to +1.50 ‰ and are all isotopically lighter than their corresponding sediment samples (Fig. 3a). In contrast, $\delta^{98}Mo_{auth}$ signatures of the graben core sediments show a wide range and greater variability between -1.39 to +2.07 ‰ (Fig. 3b) likely due to contributions from Mn oxides. Corresponding pore water samples are characterized by overall isotopically heavier $\delta^{98}Mo_{auth}$ values between +0.50 and +0.80 ‰ but are still lighter than at the OMZ site (Table 3, data repository). In the vent-related core, the sediments are characterized by $\delta^{98}Mo_{auth}$ values between +1.65 and +2.20 ‰, except the uppermost cm, where a much lighter $\delta^{98}Mo_{auth}$ value of -0.42 ‰ was measured. $\delta^{98}Mo$ signatures of pore water samples increase from +0.69 at the top to +3.15 ‰ at the bottom of the core. These values are isotopically lighter than the corresponding sediment samples in the upper part of the core but isotopically heavier in the lower part of the core (Fig. 3c).

## 6. Discussion

### 6.1. Depositional and diagenetic processes controlling Mo geochemistry

#### 6.1.1. Sedimentary Mo cycling in the graben core

The weakly oxic bottom water conditions at the graben site favor the precipitation of Mn oxides leading to elevated Mn/Al ratios relative to the continental crust background (avg. UCC of Mn/Al > 0.01, Rudnick and Gao (2003); Fig. 3b) at the core top. Within the upper 4 cm, this ratio decreases from around 1 to nearly 0 due to the reductive dissolution of Mn(VI)-oxides to aqueous Mn(II), which then accumulates in the pore waters (Fig. 3b; Table 3, data repository) (Froelich et al., 1979; Burdige, 1993). Aqueous Mn(II) can in turn diffuse upwards and be re-oxidized and precipitated, thus increasing the

335 Mn/Al ratio in the upper few cm of the core (Burdige, 1993). Since early diagenesis in the graben core
336 is dominated by Mn cycling, we apply these data to investigate Mo cycling under manganous conditions.
337 Mn oxides effectively adsorb oxymolybdate ($Mo(VI)O_4^{2-}$) from the ambient seawater (Shimmield and
338 Price, 1986) with an equilibrium fractionation factor of about -3 ‰ relative to seawater (Siebert et al.,
339 2003; Barling and Anbar, 2004; Tossell, 2005; McManus et al., 2006; Wasylenki et al., 2008;
340 Kashiwabara et al., 2011; Wasylenki et al., 2011). Based on previous findings, we suggest that the
341 transport of Mo in the sediment in oxic settings is dominated by adsorption to Mn oxides and therefore
342 the resulting sedimentary $Mo_{auth}$ isotope composition is expected to be light relative to seawater (e.g.
343 Siebert et al., 2006; Poulson-Brucker et al., 2009; Wasylenki et al., 2011; Goldberg et al., 2012; Scholz
344 et al., 2018), consistent with the observations throughout the core (Fig. 3b; Table 3, data repository).
345 Sedimentary $Mo_{auth}$ concentrations decrease in the upper 4 cm of the graben core due to dissolution of
346 Mn oxides and reach their lowest abundances coinciding with the highest concentrations of aqueous Mn
347 in the pore water between 5 and 12 cm depth. At the same depth, pore water Mo concentrations reach
348 their maximum values. Solid phase $Mo_{auth}$ isotope values are markedly low (up to -1.39 ‰) in this
349 section of the core, indicating that heavy Mo isotopes are preferentially released into the pore water
350 during dissolution of Mn oxides, which is supported by the, relatively, heavy isotope composition of the
351 pore water Mo (+0.50 to 0.80 ‰). The data also indicate that this is a non-equilibrium fractionation
352 process due to the complex early diagenetic reactions. A similar observation was made by Reitz et al.
353 (2007), who found that the $\delta^{98}$Mo signatures of Mediterranean sapropels are lighter than those of
354 hydrogenetic ferromanganese Mn-crusts, which they attributed to repeated dissolution and
355 re-precipitation of Mn oxides.
356 The highest $\delta^{98}Mo_{auth}$ values are observed at the core top (up to +2.07 ‰). Downward diffusion of
357 isotopically heavy Mo from the bottom water and quantitative precipitation within the sediment can be
358 excluded since the Mo concentration gradient in the pore water between 2 cm and 15 cm is indicative
359 of upward rather than downward transport in the upper part of the core. Therefore, a more likely
360 explanation is upward diffusion and precipitation of Mo from Mn oxide dissolution. However, the pore
361 waters have an isotope composition intermediate between the solid phase $\delta^{98}Mo_{auth}$ values observed
362 within the zone of Mn oxide dissolution and re-precipitation (+0.50 to 0.80 ‰). This observation

suggests that additional fractionation mechanisms have to be invoked to explain the heavy Mo isotope composition of +2.07 ‰ in the uppermost cm. The $\delta^{98}Mo_{PW}$ signatures are relatively constant over a broad concentration range. We observe a positive correlation ($R^2 = 0.73$) between the $\delta^{98}$Mo values of pore water and sediment in the graben core (Fig. 4a). A similar observation was made by Scholz et al. (2018) in sediments from the Baltic Sea, where large amounts of Mo are released into the pore water from Mn oxides, which had precipitated during oxygenation events in an otherwise anoxic and sulfidic water column. Following their interpretation, we suggest that the $\delta^{98}$Mo of pore waters is buffered by isotopic exchange with an adjacent solid phase pool. Due to the low concentration of Mo in the pore waters relative to the solid phase, any exchange with the solid phase will dominate the pore water Mo isotope composition.

With increasing pyritization of reactive Fe in the lower part of the core (between 12 and 32 cm, Table 3 in the data repository), Mo is quantitatively removed from the pore water and concentrations in the sedimentary solid phase increase (Fig. 3b). In this core, Mo removal takes place in the apparent absence of dissolved $H_2S$ in the pore water, as any produced $H_2S$ probably reacted with reactive Fe minerals or pore water Fe to Fe sulfide minerals and does not accumulate in the pore water (Canfield et al., 1992). The $Mo_{auth}$ isotope composition becomes increasingly heavier down core, reaching isotopically heavy $\delta^{98}Mo_{auth}$ values of up to +1.34 ‰ at the lower end of the core (Fig. 3b). This $\delta^{98}Mo_{auth}$ value is isotopically heavier than the concentration-weighted average $\delta^{98}$Mo signature of the core (+0.51 ‰). This pronounced difference between the lightest value of -1.39 ‰ in the middle section of the core and the heavy +1.34 ‰ at the base of the core argues for a separation of heavy and light Mo isotopes within the manganous zone. Repeated dissolution and reprecipitation of Mn oxides seems to retain isotopically light Mo within the surface sediments whereas isotopically heavy Mo is buried presumably associated with Fe-sulfides. Transformation of molybdate to (intermediate) thiomolybdate may also occur in the lower sediment core section, but this process is unlikely to account for the Mo isotope composition recorded within the deeper sediment, since this process would generate a shift towards lighter $\delta^{98}Mo_{auth}$ values in the solid phase. Instead, we propose that shallow Mn recycling preferentially retains the light $Mo_{auth}$ isotopes in the reactive surface sediments, whereas the buried $Mo_{auth}$ has a heavy $Mo_{auth}$ isotope composition compared to the Mo originally delivered with Mn oxides.

391

392 6.1.2. Sedimentary Mo cycling in the OMZ core

393 The low concentrations of aqueous Mn in the pore water of the OMZ core and depleted sedimentary
394 Mn/Al ratios relative to the UCC (Mn/Al < 0.01; Fig. 3a) imply reduction and dissolution of Mn oxides
395 in the water column, preventing the sedimentation of Mn oxides (Johnson et al., 1992; Johnson et al.,
396 1996). Thus, while the graben core is dominated by manganous conditions, Mn cycling is negligible in
397 the OMZ core (Fig. 3a,b). Instead, ferruginous and sulfidic conditions prevail as indicated by elevated
398 Fe and $H_2S$ concentrations, at 0 cm to 19 cm and 19 to 40 cm, respectively (Fig. 3a). This pore water
399 geochemical regime is indicative of more reducing conditions in the sediments compared to the graben
400 core. Iron is released to the pore water during reductive dissolution of Fe oxides and re-precipitates as
401 Fe-sulfide ($Fe_{Py}$) at the transition from ferruginous to sulfidic conditions (ca. 19 cm). These diagenetic
402 conditions are different compared to the graben core and are reflected by differences in the mode of Mo
403 cycling. In contrast to the isotopically light compositions in the upper 12 cm of the graben core, $\delta^{98}Mo_{auth}$
404 signatures in the upper 14 cm of the OMZ core are relatively heavy (+2.05 ± 0.11 ‰) and thus close to
405 the seawater signature of +2.34 ‰ (Barling et al., 2001; Siebert et al., 2003; Nakagawa et al., 2012).
406 The pore water Mo profile is almost linear and decreases from seawater-like concentrations at the top
407 to 5 nM at 26 cm depth. The lack of a pronounced Mo peak in the pore water suggests that Mo delivery
408 with and release from solid particles (e.g., Mn oxides) is less important than for the graben core. This
409 assumption is consistent with the interpretation that Mn oxides are already dissolved in the water
410 column. We propose that the heavy Mo isotope composition observed can be explained by diffusive
411 transport of Mo into the sediment. Such a diffusional influx can be calculated by Fick's first law of
412 diffusion:

413 $$J = -\phi \cdot D_{sed} \cdot \frac{\partial C}{\partial x}.$$

414 Here, $J$ is the diffusive flux, which is proportional to the Mo concentration depth gradient $\frac{\partial C}{\partial x}$ (in nM cm$^{-}$
415 $^{1}$). The porosity is $\phi$ and $D_{sed}$ is the diffusion coefficient of Mo in sediment pore water, which was
416 derived by adjusting the diffusion coefficient to ambient temperature (6.6 °C), salinity (35), and pressure
417 using the Stokes-Einstein equation as well as by correcting for tortuosity according to Boudreau (1996).

418 The pore water profile of aqueous Mo shows a $\frac{\partial C}{\partial x}$ gradient of -4.24 nM cm$^{-1}$ (calculated from 0.5 to 27
419 cm sediment depth; Table 2, data repository). For an average porosity of 0.92, the calculated Mo flux
420 into the sediment by diffusion from the bottom water is 0.55 nmol cm$^{-2}$ yr$^{-1}$. This value can be compared
421 to the total Mo accumulation rate in the sediment, which is calculated as the product of the average
422 $Mo_{auth}$ concentration of the solid phase (5.28 µg g$^{-1}$) and the mass accumulation rate (MAR; g cm$^{-2}$ yr$^{-1}$).
423 The mass accumulation rate was estimated from the sedimentation rate ($SR$ = 120 cm kyr$^{-1}$; approximate
424 value from Donegan and Schrader (1982)), dry bulk density ($\varphi$ = 2.4 g cm$^{-3}$; Dean et al. (2004)) and
425 porosity at the lower end of the core ($\Phi_\infty$ = 0.92)

426 $$MAR = SR \cdot \varphi(1 - \Phi_\infty).$$

427 This results in a Mo mass accumulation rate of 2.06 nmol cm$^{-2}$ yr$^{-1}$, which is higher than the calculated
428 diffusion-controlled Mo flux above (0.55 nmol cm$^{-2}$ yr$^{-1}$). Nevertheless, Mo diffusion from the bottom
429 water is clearly an important factor contributing to Mo accumulation and the relatively heavy Mo isotope
430 composition at the OMZ site.
431 We note that diffusive Mo delivery is expected to take effect at and below the depth of Mo depletion in
432 the pore water (27 cm). Moreover, the $Mo_{auth}$ isotope compositions in the upper 14 cm of the core are
433 slightly lighter than seawater (average of +2.05 ‰). Taking into account our pore water data for this
434 core, we observe that in the uppermost 2 cm of the core the aqueous Mo concentrations are higher (130
435 nM) than in the overlying bottom water (106 nM), before they decrease continuously down core. This
436 indicates an additional source of Mo at the time of sampling, likely release of Mo from particulate matter
437 at the core top. Since the Mo enrichment in the pore water coincides with an increase in dissolved Fe,
438 we hypothesize that Mo is released from Fe-(oxyhydr)oxides. Scholz et al. (2017) suggested that Mo
439 delivery with Fe oxides may be typical for OMZ environments, where Mn oxides are partly dissolved
440 in the water column. As a likely explanation for the observed features in this core we propose that
441 particulate Mo supply dominates during the summer season when sedimentation in the Gulf of California
442 is dominated by terrigenous input (Thunell et al., 1993). In contrast, diffusion from bottom water is
443 likely dominant during the productive winter season when terrigenous sedimentation and thus
444 particulate Mo supply is at its minimum.

445 Adsorption of Mo to Fe oxides involves an isotope equilibrium fractionation resulting in $\Delta^{98}Mo_{solution\text{-}Fe\text{-}oxides}$ ranging from +0.83 to +2.19 ‰, where fractionation increases with the crystallinity of the Fe oxides
447 (Goldberg et al., 2009). A particulate Mo source in the form of ferrihydrite would explain the pore water
448 Mo concentrations higher than seawater in the core top and the release of isotopically light Mo into the
449 pore water (+1.07 and +1.50 ‰) in the ferruginous zone after the deposition (Fig. 3a). The solid phase
450 shows a heavier (seawater-like) average Mo isotope composition of +2.05 ± 0.11 ‰ in the ferruginous
451 zone (0 to 14 cm). This indicates that in contrast to the graben site, heavy isotopes are preferentially
452 incorporated in the solid phase, while light isotopes remain in the pore water, likely because Mn-cycling
453 in these sediment is insignificant. Our mass-balance calculations are based on the Mo mass accumulation
454 rate and the diffusion-controlled Mo flux. The calculation of a mixed source of ferrihydrite (~60 %;
455 $\delta^{98}$Mo of +1.51 ‰) and seawater (~40 %; $\delta^{98}$Mo of +2.34 ‰) yields a Mo isotope composition of about
456 +1.86 ‰, which agrees with the average signature of +1.77 ± 0.20 ‰ measured at a depth between 14
457 to 40 cm of the OMZ site (Fig. 3a). The shift of $\delta^{98}Mo_{auth}$ to lighter values coincides with the onset of
458 pyrite/sulfide precipitation (16 cm; Fig. 3a). The isotope composition then remains relatively constant
459 further down core, even with the increasing accumulation of aqueous $H_2S$ in the pore waters below 19
460 cm depth (Fig. 3a). The accumulation of aqueous $H_2S$ coincides with the near-quantitative removal of
461 aqueous Mo and the increase of solid phase $Mo_{auth}$, which is closely coupled to the extent of pyritization
462 (Fig. 3 a). Interestingly, the shift to lighter $\delta^{98}Mo_{auth}$ signatures and the precipitation of pyrite is observed
463 at 15-19 cm and thus slightly above the complete removal of pore water Mo and the accumulation of
464 pore water $H_2S$ (Fig. 3a). This might be explained by a sulfidation-induced speciation change of
465 molybdate or Mo adsorption to or sequestration into pyrite (Helz et al., 1996; Erickson and Helz, 2000;
466 Poulson-Brucker et al., 2012). Any $H_2S$ generated by bacterial sulfate reduction at this depth (15 to 17.5
467 cm) is likely removed through precipitation of Fe sulfide minerals from pore water Fe and reactive Fe
468 minerals (Canfield et al., 1992) and is thus not accumulated in the pore water yet.
469
470 6.1.3. Sedimentary Mo cycling in the vent-related core
471 The vent-related core consists of black smoker debris, which is a heterogeneous mix of metal-rich oxide
472 and sulfide (pyrrhotin, pyrite, Zn- and Cu-sulfides) minerals (Francheteau et al., 1979; Fig. 3c; e.g. Alt

et al., 1987; Berndt et al., 2016). The overlying bottom waters are weakly oxic, similar to the location of the graben core described above. Below the hemipelagic surface layer, elevated aqueous Mn concentrations indicate reductive dissolution of Mn oxides coupled to upward diffusion and re-precipitation. Aqueous Mn concentrations are tightly coupled to aqueous Mo concentrations as visible in Fig. 3c, indicating that Mo is released into the pore waters from dissolving Mn oxides. Consistent with this notion, the pore water and solid phase of the uppermost sample show the lightest $\delta^{98}Mo_{auth}$ signatures of the core.

Below the surface layer, ferruginous conditions prevail and $Mo_{auth}$ concentrations in the solid phase generally increase with depth. We observe a marked correlation between $Mo_{auth}$ and Zn concentrations in the solid phase ($R^2 = 0.89$) (Fig. 4b), which indicates that $Mo_{auth}$ was incorporated into the solid phase during the formation of the original vent edifices (Trefry et al., 1994; Metz and Trefry, 2000; Seyfried et al., 2004). Based on mineral assemblages and direct measurements, the formation temperature of these vents (i.e. the temperature of the hydrothermal fluid end member) was estimated to be around 300 °C (Kastner, 1982; von Damm et al., 1985; Zierenberg et al., 1994; Berndt et al., 2016). In this temperature range, Mo is effectively scavenged by vent-minerals from the ambient vent fluid in the presence of sulfide and precipitates as a high-T sulfide phase (Metz and Trefry, 2000; Seyfried et al., 2004). Molybdenum fixation probably takes place with little isotope fractionation due to the high temperatures prevailing. The heavy $Mo_{auth}$ isotope composition of the sediment in the core (+1.94 ± 0.34 ‰) may imply that the main Mo source of the vent fluid is seawater. The slight shift towards lighter $Mo_{auth}$ isotope compositions than that of seawater can be explained by fluid-sediment interactions during transport of the hydrothermal fluid through the black smoker chimney and sediments, e.g. sulfidation-induced speciation changes (McManus et al., 2002; Tribovillard et al., 2004; Nägler et al., 2011). To summarize, we suggest that only the uppermost layer of the core does show a strong diagenetic signal and that the Mo isotope composition close to seawater in the lower part of the core is “inherited” from the original smoker material that forms the debris. Nevertheless, this interpretation does not explain the very heavy pore water Mo isotope compositions in the lower part of the core. Secondary diagenetic processes might lead to a preferential incorporation of light Mo from the pore water into the solid phase

here. However, we do not have enough pore water isotope data to conclusively interpret this particular feature.

### 6.2. Comparison of Mo systematics in anoxic continental margin sediments of the Guaymas Basin and the Peruvian margin

The systematic differences in Mo geochemistry and Mo isotope behavior observed in the investigated cores show that the sedimentary composition is strongly controlled by (1) the transport mechanisms of Mo from the overlying bottom water to the sediment and (2) subsequent interaction of the solid phase with the ambient pore water. Molybdenum delivered to the sediment via diffusion from the bottom waters results in an isotopically heavy composition of the solid phase close to seawater. Pore water concentrations are close to the bottom water/seawater concentration (~100-110 nM) and gradually decrease downcore (Fig. 3a). The diffusive transport implied by such a pore water profile influences the $\delta^{98}$Mo signature of the Guaymas OMZ core. On the other hand, Mo transport to the sediment by adsorption onto particulate matter, e.g. Mn and Fe oxides with a variably light Mo isotopic composition and release during reductive dissolution of these particulate phases in the sediment results in light isotopic compositions of the solid phase (Fig. 3b,c). Particulate Mo supply can be identified by higher Mo concentrations in pore waters compared to the bottom waters and dominates the graben core as well as, to a lesser extent, the vent-related core. Following these initial supply mechanisms, Mo is incorporated into Fe-sulfides, which is likely accompanied by isotopic fractionation due to non-quantitative sequestration of Mo (e.g. Tossell, 2005; Goldberg et al., 2009; Kerl et al., 2017).

In contrast to the heavy Mo isotope composition observed in the OMZ core of the Guaymas Basin, sediment samples from the OMZ along the Peruvian margin (<300 m water depth) (Scholz et al., 2011), show lighter $\delta^{98}Mo_{auth}$ signatures and higher $Mo_{auth}$ concentrations (Fig. 4c) (Scholz et al., 2017). Samples from the Peruvian margin were shown to be dominated by particulate Mo transport to the sediment, presumably via Fe oxides (Scholz et al., 2017). The $\delta^{98}Mo_{auth}$ of Peru margin sediments (+1.32 ± 0.17 ‰) is similar to the lower end of the particle-dominated Guaymas graben core (+1.34 ‰) and significantly lighter than the diffusion-dominated Guaymas OMZ core (+1.93 ± 0.32 ‰). Pore waters in the uppermost ca. 15 cm of Peruvian shelf sediments have aqueous Mo concentrations >110 nM

528 (Scholz et al., 2017), similar to the particle-dominated graben core in the Guaymas Basin. As a result of
529 the particle based transport mechanism, Mo accumulation rates in Peruvian shelf sediments are
530 significantly higher (16.2 nmol $cm^{-2}$ $yr^{-1}$ (Scholz et al., 2011)) than in sediments within the Guaymas
531 Basin OMZ (2.06 nmol $cm^{-2}$ $yr^{-1}$) (Fig. 5). These observations imply that the $Mo_{auth}$ isotope composition
532 of sediments deposited in anoxic bottom waters is generally dependent on conditions that induce either
533 particle-dominated or diffusion-influenced Mo supply (Fig. 5).
534 These fundamentally different modes of Mo delivery in continental margin settings result from distinct
535 environmental and depositional conditions. The Peruvian OMZ is located between <50 to about 500 m
536 water depth (Scholz et al., 2011). The average primary production off Peru is about 350 g C $m^{-2}$ $yr^{-1}$
537 (Muller and Suess, 1979) and a large fraction of the organic material exported reaches the surface
538 sediments (TOC accumulation rates on the shelf range from 30-60 g C $m^{-2}$ $yr^{-1}$) (Scholz et al., 2011;
539 Dale et al., 2015). The high organic matter flux along the Peruvian shelf combined with sluggish
540 ventilation induces a strongly reducing environment due to high rates of anaerobic respiration. This is
541 reflected by intense denitrification in the Peruvian OMZ (Lam et al., 2009b; Thamdrup et al., 2012), and
542 the episodic occurrence of hydrogen sulfide in the bottom water (Schunck et al., 2013; Scholz et al.,
543 2016). Scholz et al. (2017) proposed that repeated cycles of reduced Fe oxide dissolution in the surface
544 sediment, sedimentary Fe release and re-precipitation in the bottom waters provide a highly efficient
545 transport mechanism of particle-bound Mo to the sediment explaining high Mo accumulation rates (Fig.
546 5). Adsorption to and transport of isotopically light Mo with organic matter may represent another
547 particulate Mo-shuttle to the sediment (Tribovillard et al., 2004; Ho et al., 2018; King et al., 2018). Such
548 a scenario would be consistent with Mo-TOC covariation in the sediment (Figure 6a). On the other hand
549 high rates of organic carbon accumulation drive intense bacterial sulfate reduction (Bohlen et al., 2012)
550 and Mo fixation in the sediment with hydrogen sulfide. Therefore, Mo-TOC co-variation would also be
551 indirect, which is supported by the co-variation of total organic carbon (TOC), total sulfur (TS) and Mo
552 concentrations in OMZ sediments of the Peruvian margin and the Guaymas Basin (Fig. 6a-c).
553 The Gulf of California OMZ is located at about 500 to 1000 m water depth (Wyrtki, 1962; Bray, 1988;
554 Thunell, 1998) and is therefore significantly deeper than the Peruvian OMZ (Fig. 5). The average
555 primary production is lower than above the Peruvian shelf, at about 130 g C $m^{-2}$ $yr^{-1}$ (Brumsack, 1989)

556 and a larger fraction of the organic material exported is re-mineralized in the water column prior to
557 deposition at the seafloor (TOC accumulation rates are of the order of 5.6 g C $m^{-2}$ $yr^{-1}$ based on an
558 average TOC content of 3.3 wt-% and the MARs used in section 6.1.2). Sinking organic matter
559 originating from shallower depths is probably mostly degraded in the oxygenated water column before
560 deposition on the seafloor underneath the deeper OMZ. Furthermore, due to the steeper slope topography
561 underneath the Guaymas Basin OMZ, Fe released from the sediment is mainly transported downslope
562 and into the basin rather than being repeatedly recycled at the same site (Scholz et al., 2019). It is thus
563 unlikely that multiple cycles of Fe dissolution in the sediment and re-precipitation in the bottom water
564 accelerate Mo accumulation. Thus, although Mo supply via particulate matter is the dominant process
565 in the Guaymas Basin OMZ, diffusion from the bottom water contributes significantly to the overall Mo
566 mass accumulation rate. The relatively low TOC content in the sediment also limits sulfide production
567 thus leading to Mo removal at greater sediment depth. Therefore, the retention of the Mo supplied by
568 particulate matter is less efficient compared to the Peruvian OMZ resulting in an overall lower Mo mass
569 accumulation rate (Fig. 6).
570
571 6.3. Implications for the applications of the Mo isotope redox proxy in marine anoxic settings
572 A wide range of $\delta^{98}$Mo signatures that have been observed in open-marine anoxic settings (anoxic
573 "OMZ" sediments in Fig. 7) in previous studies (McManus et al., 2006; Poulson et al., 2006; Siebert et
574 al., 2006; Poulson-Brucker et al., 2009). Our findings for modern, well constrained marine settings
575 suggest that this variability can be explained by different supply mechanisms of Mo to the sediment. In
576 these previous studies light Mo isotope compositions were attributed to isotope fractionation on Mn-Fe
577 oxides (Poulson et al., 2006; Siebert et al., 2006) while heavier Mo isotope compositions were attributed
578 to fractionation processes associated with sedimentary sulfide formation (Poulson et al., 2006; Siebert
579 et al., 2006; Poulson-Brucker et al., 2009). Furthermore, McManus et al. (2006) and Siebert et al. (2006)
580 suggested that Mo accumulation is indirectly coupled to organic carbon burial, which drives sedimentary
581 sulfate reduction. Our new findings in combination with those of Scholz et al. (2017) complement these
582 earlier studies and add distinctive Mo isotope compositions associated with transport mechanisms of
583 Mo to the sediment. We can demonstrate that a shallow OMZ with high rates of organic carbon

584 accumulation such as the Peruvian OMZ promotes intense particulate Mo supply with a light isotope
585 composition, as well as efficient sedimentary Mo fixation with hydrogen sulfide. In contrast,
586 significantly lower particulate Mo supply in a deeper and steeper slope environment favors diffusive
587 Mo supply to the sediments originating from the overlying bottom water. This improved understanding
588 of Mo cycling in open-marine anoxic environments is important for the interpretation of Mo contents
589 and isotope compositions of paleo-records. On a local scale, the Mo isotope composition of the
590 sediments is known to be affected by early diagenetic processes, such as Mo release from and re-
591 adsorption to Mn oxides (Reitz et al., 2007 and this study). In this context, a recent study by Kurzweil
592 et al. (2016) shows a Mo isotope data set implying that a Mn oxide shuttling may have been operating
593 even before the Great oxidation event. As shown in our study, the deposition of particulate material
594 other than Mn oxides, also significantly contributes to Mo accumulation and the sedimentary Mo isotope
595 composition in anoxic open-marine settings (Fig. 7). A change in the mode of Mo delivery may result
596 in a wide range of Mo contents and isotope compositions within the same core (Figs. 1, 3a, 3c). This
597 means that paleo-records with variable Mo concentrations and isotope signatures do not necessarily
598 imply major redox-changes such as a transition from oxic to euxinic conditions in the water-column but
599 may rather reflect changes in the mode of Mo delivery. This means that other lithological and
600 geochemical information has to be combined with the Mo redox proxy to obtain realistic interpretations.
601 It also means that future mass balance modelling of the different Mo reservoirs, sources and sinks on a
602 global scale needs to consider the effects of particulate versus diffusive Mo delivery.
603
604 **7. Summary and conclusions**
605 In this study, we investigated three sites in the Guaymas Basin, Gulf of California, which differ in their
606 depositional environment and redox conditions. Molybdenum concentrations and isotope compositions
607 of solids and pore waters of these sites reflect distinct supply mechanisms of Mo to the sediment:
608 • Sediments from the OMZ show evidence of Mo supply via two mechanisms, Fe-oxide particulates
609 and diffusion from bottom water.
610 • Sediments from the oxic graben site reflect Mo supply via Mn oxide particulates.

- Sediments near a hydrothermal vent field are mainly affected by Mo removal from seawater with Fe-Zn-Cu-sulfides at high temperatures.

Dissolution and precipitation processes during early sediment diagenesis further affect the content and isotopic composition of Mo. Reductive dissolution and re-precipitation of Mn oxides within the surface sediments preferentially recycles the light Mo isotopes thus generating a burial flux that is isotopically heavier than the Mo supplied by Mn oxides. In contrast, incomplete Mo sequestration by sulfide phases generates a shift towards lighter Mo isotope values compared to the Mo originally delivered by solid particles or via diffusion. In summary, our data imply that paleo-records showing heavy (seawater-like) $\delta^{98}$Mo signatures and low Mo contents reflect a Mo supply that is influenced by diffusion from overlying bottom waters to the sediments. In contrast, lighter $\delta^{98}$Mo signatures and generally higher but variable Mo contents (Fig. 7) reflect Mo supply with particulate matter. High TOC rain rates drive intense sulfide production in the sediment thus favoring Mo fixation and burial over Mo recycling. In settings with high particulate Mo supply, the balance between Mo delivery and burial versus recycling determines the Mo concentration and isotope composition recorded in the sedimentary archive. We propose that the concepts outlined in our study are applicable to interpret the Mo isotope variability in the paleo-record of open-marine systems in terms of environmental conditions and changes.

**Acknowledgement**

We thank the government of Mexico for granting access to their territorial waters as well as the captain and crew of R.V. Sonne for their support during cruise SO241. We thank C. Hensen, S. Geilert, and A. Fiskal for support during sampling as well as A. Beck, A. Bleyer, B. Domeyer, J. Heinze, A. Retschko, and R. Surberg for technical and analytical assistance. The comments and suggestions of the executive editor J. Catalano, associate editor S. Severmann and three anonymous reviewers helped to improve the manuscript. This study was supported by the German Research Foundation (DFG) through Sonderforschungsbereich 754 ("Climate-Biogeochemistry Interactions in the Tropical Ocean") and the Emmy Noether Nachwuchsforschergruppe ICONOX ("Iron Cycling in Continental Margin Sediments and the Nutrient and Oxygen Balance of the Ocean").

## References


Alt, J.C., Lonsdale, P., Haymon, R. and Muehlenbachs, K. (1987) Hydrothermal Sulfide and Oxide Deposits on Seamounts near 21-Degrees-N, East Pacific Rise. Geol Soc Am Bull 98, 157-168.

Archer, C. and Vance, D. (2008) The isotopic signature of the global riverine molybdenum flux and anoxia in the ancient oceans. Nat Geosci 1, 597-600.

Arnold, G.L., Anbar, A.D., Barling, J. and Lyons, T.W. (2004) Molybdenum isotope evidence for widespread anoxia in mid-proterozoic oceans. Science 304, 87-90.

Barling, J. and Anbar, A.D. (2004) Molybdenum isotope fractionation during adsorption by manganese oxides. Earth Planet Sc Lett 217, 315-329.

Barling, J., Arnold, G.L. and Anbar, A.D. (2001) Natural mass-dependent variations in the isotopic composition of molybdenum. Earth Planet Sc Lett 193, 447-457.

Berndt, C., Hensen, C., Mortera-Gutierrez, C., Sarkar, S., Geilert, S., Schmidt, M., Liebetrau, V., Kipfer, R., Scholz, F., Doll, M., Muff, S., Karstens, J., Planke, S., Petersen, S., Bottner, C., Chi, W.C., Moser, M., Behrendt, R., Fiskal, A., Lever, M.A., Su, C.C., Deng, L., Brennwald, M.S. and Lizarralde, D. (2016) Rifting under steam-How rift magmatism triggers methane venting from sedimentary basins. Geology 44, 767-770.

Bertine, K.K. and Turekian, K.K. (1973) Molybdenum in Marine Deposits. Geochim Cosmochim Ac 37, 1415-1434.

Bigeleisen, J. and Mayer, M.G. (1947) Calculation of Equilibrium Constants for Isotopic Exchange Reactions. J Chem Phys 15, 261-267.

Bohlen, L., Dale, A.W. and Wallmann, K. (2012) Simple transfer functions for calculating benthic fixed nitrogen losses and C:N:P regeneration ratios in global biogeochemical models. Global Biogeochem Cy 26.

Boning, P., Brumsack, H.J., Bottcher, M.E., Schnetger, B., Kriete, C., Kallmeyer, J. and Borchers, S.L. (2004) Geochemistry of Peruvian near-surface sediments. Geochim Cosmochim Ac 68, 4429-4451.

Bostick, B.C., Fendorf, S. and Helz, G.R. (2003) Differential adsorption of molybdate and tetrathiomolybdate on pyrite (FeS2). Environ Sci Technol 37, 285-291.

Boudreau, B.P. (1996) The diffusive tortuosity of fine-grained unlithified sediments. Geochim Cosmochim Ac 60, 3139-3142.

Bray, N.A. (1988) Water Mass Formation in the Gulf of California. J Geophys Res-Oceans 93, 9223-9240.

Brumsack, H.J. (1989) Geochemistry of Recent Toc-Rich Sediments from the Gulf of California and the Black-Sea. Geol Rundsch 78, 851-882.

Burdige, D.J. (1993) The Biogeochemistry of Manganese and Iron Reduction in Marine-Sediments. Earth-Sci Rev 35, 249-284.

Calvert, S.E. (1966) Origin of Diatom-Rich Varved Sediments from Gulf of California. J Geol 74, 546-&.

Calvert, S.E. and Pedersen, T.F. (1993) Geochemistry of Recent Oxic and Anoxic Marine-Sediments - Implications for the Geological Record. Mar Geol 113, 67-88.

Canfield, D.E., Raiswell, R. and Bottrell, S. (1992) The Reactivity of Sedimentary Iron Minerals toward Sulfide. Am J Sci 292, 659-683.

Canfield, D.E. and Thamdrup, B. (2009) Towards a consistent classification scheme for geochemical environments, or, why we wish the term 'suboxic' would go away. Geobiology 7, 385-392.

Chappaz, A., Lyons, T.W., Gregory, D.D., Reinhard, C.T., Gill, B.C., Li, C. and Large, R.R. (2014) Does pyrite act as an important host for molybdenum in modern and ancient euxinic sediments? Geochim Cosmochim Ac 126, 112-122.

Chever, F., Rouxel, O.J., Croot, P.L., Ponzevera, E., Wuttig, K. and Auro, M. (2015) Total dissolvable and dissolved iron isotopes in the water column of the Peru upwelling regime. Geochim Cosmochim Ac 162, 66-82.

Cline, J.D. (1969) Spectrophotometric Determination of Hydrogen Sulfide in Natural Waters. Limnol Oceanogr 14, 454-&.

Collier, R.W. (1985) Molybdenum in the Northeast Pacific-Ocean. Limnol Oceanogr 30, 1351-1354.

690 Crusius, J., Calvert, S., Pedersen, T. and Sage, D. (1996) Rhenium and molybdenum enrichments in
691 sediments as indicators of oxic, suboxic and sulfidic conditions of deposition. Earth Planet Sc Lett
692 145, 65-78.
693 Dahl, T.W., Anbar, A.D., Gordon, G.W., Rosing, M.T., Frei, R. and Canfield, D.E. (2010) The behavior of
694 molybdenum and its isotopes across the chemocline and in the sediments of sulfidic Lake Cadagno,
695 Switzerland. Geochim Cosmochim Ac 74, 144-163.
696 Dahl, T.W., Chappaz, A., Fitts, J.P. and Lyons, T.W. (2013) Molybdenum reduction in a sulfidic lake:
697 Evidence from X-ray absorption fine-structure spectroscopy and implications for the Mo paleoproxy.
698 Geochim Cosmochim Ac 103, 213-231.
699 Dahl, T.W., Chappaz, A., Hoek, J., McKenzie, C.J., Svane, S. and Canfield, D.E. (2017) Evidence of
700 molybdenum association with particulate organic matter under sulfidic conditions. Geobiology 15,
701 311-323.
702 Dale, A.W., Sommer, S., Lomnitz, U., Montes, I., Treude, T., Liebetrau, V., Gier, J., Hensen, C., Dengler,
703 M., Stolpovsky, K., Bryant, L.D. and Wallmann, K. (2015) Organic carbon production, mineralisation
704 and preservation on the Peruvian margin. Biogeosciences 12, 1537-1559.
705 Dalsgaard, T., Thamdrup, B., Farias, L. and Revsbech, N.P. (2012) Anammox and denitrification in the
706 oxygen minimum zone of the eastern South Pacific. Limnol Oceanogr 57, 1331-1346.
707 Dean, W., Pride, C. and Thunell, R. (2004) Geochemical cycles in sediments deposited on the slopes
708 of the Guaymas and Carmen Basins of the Gulf of California over the last 180 years. Quaternary Sci
709 Rev 23, 1817-1833.
710 Dellwig, O., Bottcher, M.E., Lipinski, M. and Brumsack, H.J. (2002) Trace metals in Holocene coastal
711 peats and their relation to pyrite formation (NW Germany). Chem Geol 182, 423-442.
712 Donegan, D. and Schrader, H. (1982) Biogenic and Abiogenic Components of Laminated Hemipelagic
713 Sediments in the Central Gulf of California. Mar Geol 48, 215-237.
714 Emerson, S.R. and Huested, S.S. (1991) Ocean Anoxia and the Concentrations of Molybdenum and
715 Vanadium in Seawater. Mar Chem 34, 177-196.
716 Erickson, B.E. and Helz, G.R. (2000) Molybdenum(VI) speciation in sulfidic waters: Stability and lability
717 of thiomolybdates. Geochim Cosmochim Ac 64, 1149-1158.
718 Francheteau, J., Needham, H.D., Choukroune, P., Juteau, T., Seguret, M., Ballard, R.D., Fox, P.J.,
719 Normark, W., Carranza, A., Cordoba, D., Guerrero, J., Rangin, C., Bougault, H., Cambon, P. and
720 Hekinian, R. (1979) Massive Deep-Sea Sulfide Ore-Deposits Discovered on the East Pacific Rise.
721 Nature 277, 523-528.
722 Froelich, P.N., Klinkhammer, G.P., Bender, M.L., Luedtke, N.A., Heath, G.R., Cullen, D., Dauphin, P.,
723 Hammond, D., Hartman, B. and Maynard, V. (1979) Early Oxidation of Organic-Matter in Pelagic
724 Sediments of the Eastern Equatorial Atlantic - Suboxic Diagenesis. Geochim Cosmochim Ac 43, 1075-
725 1090.
726 Gieskes, J.M., Kastner, M., Einsele, G., Kelts, K. and Niemitz, J. (1982) Hydrothermal Activity in the
727 Guaymas Basin, Gulf of California - a Synthesis. Initial Rep Deep Sea 64, 1159-1167.
728 Goldberg, T., Archer, C., Vance, D. and Poulton, S.W. (2009) Mo isotope fractionation during
729 adsorption to Fe (oxyhydr)oxides. Geochim Cosmochim Ac 73, 6502-6516.
730 Goldberg, T., Archer, C., Vance, D., Thamdrup, B., McAnena, A. and Poulton, S.W. (2012) Controls on
731 Mo isotope fractionations in a Mn-rich anoxic marine sediment, Gullmar Fjord, Sweden. Chem Geol
732 296, 73-82.
733 Goldberg, T., Gordon, G., Izon, G., Archer, C., Pearce, C.R., McManus, J., Anbar, A.D. and Rehkamper,
734 M. (2013) Resolution of inter-laboratory discrepancies in Mo isotope data: an intercalibration. J Anal
735 Atom Spectrom 28, 724-735.
736 Greber, N.D., Siebert, C., Nagler, T.F. and Pettke, T. (2012) d98/95Mo values and Molybdenum
737 Concentration Data for NIST SRM 610, 612 and 3134: Towards a Common Protocol for Reporting Mo
738 Data. Geostand Geoanal Res 36, 291-300.
739 Hawco, N.J., Ohnemus, D.C., Resing, J.A., Twining, B.S. and Saito, M.A. (2016) A dissolved cobalt
740 plume in the oxygen minimum zone of the eastern tropical South Pacific. Biogeosciences 13, 5697-
741 5717.

742 Helz, G.R., Erickson, B.E. and Vorlicek, T.P. (2014) Stabilities of thiomolybdate complexes of iron;
743 implications for retention of essential trace elements (Fe, Cu, Mo) in sulfidic waters. Metallomics 6,
744 1131-1140.
745 Helz, G.R., Miller, C.V., Charnock, J.M., Mosselmans, J.F.W., Pattrick, R.A.D., Garner, C.D. and
746 Vaughan, D.J. (1996) Mechanism of molybdenum removal from the sea and its concentration in black
747 shales: EXAFS evidence. Geochim Cosmochim Ac 60, 3631-3642.
748 Ho, P., Lee, J.M., Heller, M.I., Lam, P.J. and Shiller, A.M. (2018) The distribution of dissolved and
749 particulate Mo and V along the US GEOTRACES East Pacific Zonal Transect (GP16): The roles of oxides
750 and biogenic particles in their distributions in the oxygen deficient zone and the hydrothermal plume.
751 Mar Chem 201, 242-255.
752 Huerta-Diaz, M.A. and Morse, J.W. (1992) Pyritization of Trace-Metals in Anoxic Marine-Sediments.
753 Geochim Cosmochim Ac 56, 2681-2702.
754 Johnson, K.S., Berelson, W.M., Coale, K.H., Coley, T.L., Elrod, V.A., Fairey, W.R., Iams, H.D., Kilgore,
755 T.E. and Nowicki, J.L. (1992) Manganese Flux from Continental-Margin Sediments in a Transect
756 through the Oxygen Minimum. Science 257, 1242-1245.
757 Johnson, K.S., Coale, K.H., Berelson, W.M. and Gordon, R.M. (1996) On the formation of the
758 manganese maximum in the oxygen minimum. Geochim Cosmochim Ac 60, 1291-1299.
759 Kalvelage, T., Lavik, G., Lam, P., Contreras, S., Arteaga, L., Loscher, C.R., Oschlies, A., Paulmier, A.,
760 Stramma, L. and Kuypers, M.M.M. (2013) Nitrogen cycling driven by organic matter export in the
761 South Pacific oxygen minimum zone. Nat Geosci 6, 228-234.
762 Kashiwabara, T., Takahashi, Y., Tanimizu, M. and Usui, A. (2011) Molecular-scale mechanisms of
763 distribution and isotopic fractionation of molybdenum between seawater and ferromanganese
764 oxides. Geochim Cosmochim Ac 75, 5762-5784.
765 Kastner, M. (1982) Evidence for Two Distinct Hydrothermal Systems in the Guaymas Basin, in: Curray,
766 J.R., Moore, D.G. (Eds.), Initial Rep Deep Sea. G.S. Govt. Printing Office, Washington, pp. 1143-1157.
767 Kerl, C.F., Lohmayer, R., Bura-Nakic, E., Vance, D. and Planer-Friedrich, B. (2017) Experimental
768 Confirmation of Isotope Fractionation in Thiomolybdates Using Ion Chromatographic Separation and
769 Detection by Multicollector ICPMS. Anal Chem 89, 3123-3129.
770 King, E.K., Perakis, S.S. and Pett-Ridge, J.C. (2018) Molybdenum isotope fractionation during
771 adsorption to organic matter. Geochim Cosmochim Ac 222, 584-598.
772 Kurzweil, F., Wille, M., Gantert, N., Beukes, N.J. and Schoenberg, R. (2016) Manganese oxide shuttling
773 in pre-GOE oceans - evidence from molybdenum and iron isotopes. Earth Planet Sc Lett 452, 69-78.
774 Lam, P., Lavik, G., Jensen, M., van de Vossenbergb, J., Schmid, M., Woebken, D., Gutierrez, D.,
775 Amann, R., Jetten, M. and Kuypers, M.M. (2009a) Revising the nitrogen cycle in the Peruvian oxygen
776 minimum zone. PNAS 106, 4752-4757.
777 Lam, P., Lavik, G., Jensen, M.M., van de Vossenberg, J., Schmid, M., Woebken, D., Dimitri, G., Amann,
778 R., Jetten, M.S.M. and Kuypers, M.M.M. (2009b) Revising the nitrogen cycle in the Peruvian oxygen
779 minimum zone. P Natl Acad Sci USA 106, 4752-4757.
780 McManus, J., Berelson, W.M., Severmann, S., Poulson, R.L., Hammond, D.E., Klinkhammer, G.P. and
781 Holm, C. (2006) Molybdenum and uranium geochemistry in continental margin sediments:
782 Paleoproxy potential. Geochim Cosmochim Ac 70, 4643-4662.
783 McManus, J., Nagler, T.F., Siebert, C., Wheat, C.G. and Hammond, D.E. (2002) Oceanic molybdenum
784 isotope fractionation: Diagenesis and hydrothermal ridge-flank alteration. Geochem Geophy Geosy 3.
785 Metz, S. and Trefry, J.H. (2000) Chemical and mineralogical influences on concentrations of trace
786 metals in hydrothermal fluids. Geochim Cosmochim Ac 64, 2267-2279.
787 Miller, C.A., Peucker-Ehrenbrink, B., Walker, B.D. and Marcantonio, F. (2011) Re-assessing the surface
788 cycling of molybdenum and rhenium. Geochim Cosmochim Ac 75, 7146-7179.
789 Moore, D.G. (1973) Plate-Edge Deformation and Crustal Growth, Gulf-of-California Structural
790 Province. Geol Soc Am Bull 84, 1883-1905.
791 Morford, J.L. and Emerson, S. (1999) The geochemistry of redox sensitive trace metals in sediments.
792 Geochim Cosmochim Ac 63, 1735-1750.
793 Muller, P.J. and Suess, E. (1979) Productivity, Sedimentation-Rate, and Sedimentary Organic-Matter
794 in the Oceans .1. Organic-Carbon Preservation. Deep-Sea Res 26, 1347-1362.

Nägler, T.F., Anbar, A.D., Archer, C., Goldberg, T., Gordon, G.W., Greber, N.D., Siebert, C., Sohrin, Y. and Vance, D. (2014) Proposal for an International Molybdenum Isotope Measurement Standard and Data Representation. Geostand Geoanal Res 38, 149-151.
Nägler, T.F., Neubert, N., Bottcher, M.E., Dellwig, O. and Schnetger, B. (2011) Molybdenum isotope fractionation in pelagic euxinia: Evidence from the modern Black and Baltic Seas. Chem Geol 289, 1-11.
Nakagawa, Y., Takano, S., Firdaus, M.L., Norisuye, K., Hirata, T., Vance, D. and Sohrin, Y. (2012) The molybdenum isotopic composition of the modern ocean. Geochem J 46, 131-141.
Noffke, A., Hensen, C., Sommer, S., Scholz, F., Bohlen, L., Mosch, T., Graco, M. and Wallmann, K. (2012) Benthic iron and phosphorus fluxes across the Peruvian oxygen minimum zone. Limnol Oceanogr 57, 851-867.
Pennington, J.T., Mahoney, K.L., Kuwahara, V.S., Kolber, D.D., Calienes, R. and Chavez, F.P. (2006) Primary production in the eastern tropical Pacific: A review. Prog Oceanogr 69, 285-317.
Poulson-Brucker, R.L.P., McManus, J. and Poulton, S.W. (2012) Molybdenum isotope fractionations observed under anoxic experimental conditions. Geochem J 46, 201-209.
Poulson-Brucker, R.L.P., McManus, J., Severmann, S. and Berelson, W.M. (2009) Molybdenum behavior during early diagenesis: Insights from Mo isotopes. Geochem Geophy Geosy 10.
Poulson, R.L., Siebert, C., McManus, J. and Berelson, W.M. (2006) Authigenic molybdenum isotope signatures in marine sediments. Geology 34, 617-620.
Poulton, S.W. and Canfield, D.E. (2005) Development of a sequential extraction procedure for iron: implications for iron partitioning in continentally derived particulates. Chem Geol 214, 209-221.
Raiswell, R. and Plant, J. (1980) The Incorporation of Trace-Elements into Pyrite during Diagenesis of Black Shales, Yorkshire, England. Econ Geol 75, 684-699.
Reitz, A., Wille, M., Nagler, T.F. and de Lange, G.J. (2007) Atypical Mo isotope signatures in eastern Mediterranean sediments. Chem Geol 245, 1-8.
Rudnick, R.L. and Gao, S. (2003) Composition of the Continental Crust, in: Rudnick, R.L., Holland, H.D., Turekian, K.K. (Eds.), The Crust: Treatise on Geochemistry. Elsevier-Pergamum, Oxford, pp. 1-64.
Scholz, F., Baum, M., Siebert, C., Eroglu, S., Dale, A.W., Naumann, M. and Sommer, S. (2018) Sedimentary molybdenum cycling in the aftermath of seawater inflow to the intermittently euxinic Gotland Deep, Central Baltic Sea. Chem Geol 491, 27-38.
Scholz, F., Hensen, C., Noffke, A., Rohde, A., Liebetrau, V. and Wallmann, K. (2011) Early diagenesis of redox-sensitive trace metals in the Peru upwelling area - response to ENSO-related oxygen fluctuations in the water column. Geochim Cosmochim Ac 75, 7257-7276.
Scholz, F., Loscher, C.R., Fiskal, A., Sommer, S., Hensen, C., Lomnitz, U., Wuttig, K., Gottlicher, J., Kossel, E., Steininger, R. and Canfield, D.E. (2016) Nitrate-dependent iron oxidation limits iron transport in anoxic ocean regions. Earth Planet Sc Lett 454, 272-281.
Scholz, F., McManus, J., Mix, A.C., Hensen, C. and Schneider, R.R. (2014) The impact of ocean deoxygenation on iron release from continental margin sediments. Nat Geosci 7, 433-437.
Scholz, F., Schmidt, M., Hensen, C., Eroglu, S., Geilert, S., Gutjahr, M. and Liebetrau, V. (2019) Shelf-to-basin iron shuttle in the Guaymas Basin, Gulf of California. Geochim Cosmochim Ac 261, 76-92.
Scholz, F., Siebert, C., Dale, A.W. and Frank, M. (2017) Intense molybdenum accumulation in sediments underneath a nitrogenous water column and implications for the reconstruction of paleo-redox conditions based on molybdenum isotopes. Geochim Cosmochim Ac 213, 400-417.
Schunck, H., Lavik, G., Desai, D.K., Grosskopf, T., Kalvelage, T., Loscher, C.R., Paulmier, A., Contreras, S., Siegel, H., Holtappels, M., Rosenstiel, P., Schilhabel, M.B., Graco, M., Schmitz, R.A., Kuypers, M.M.M. and LaRoche, J. (2013) Giant Hydrogen Sulfide Plume in the Oxygen Minimum Zone off Peru Supports Chemolithoautotrophy. Plos One 8.
Scott, C., Lyons, T.W., Bekker, A., Shen, Y., Poulton, S.W., Chu, X. and Anbar, A.D. (2008) Tracing the stepwise oxygenation of the Proterozoic ocean. Nature 452, 456-U455.
Seyfried, W.E., Seewald, J.S., Berndt, M.E., Ding, K. and Foustoukos, D.I. (2004) Chemistry of hydrothermal vent fluids from the Main Endeavour Field, northern Juan de Fuca Ridge: Geochemical controls in the aftermath of June 1999 seismic events (vol 108, pg 2429, 2003). J Geophys Res-Sol Ea 109.

Shimmield, G.B. and Price, N.B. (1986) The Behavior of Molybdenum and Manganese during Early Sediment Diagenesis - Offshore Baja-California, Mexico. Mar Chem 19, 261-280.
Siebert, C., McManus, J., Bice, A., Poulson, R. and Berelson, W.M. (2006) Molybdenum isotope signatures in continental margin marine sediments. Earth Planet Sc Lett 241, 723-733.
Siebert, C., Nagler, T.F. and Kramers, J.D. (2001) Determination of molybdenum isotope fractionation by double-spike multicollector inductively coupled plasma mass spectrometry. Geochem Geophy Geosy 2, art. no.-2000GC000124.
Siebert, C., Nagler, T.F., von Blanckenburg, F. and Kramers, J.D. (2003) Molybdenum isotope records as a potential new proxy for paleoceanography. Earth Planet Sc Lett 211, 159-171.
Sommer, S., Gier, J., Treude, T., Lomnitz, U., Dengler, M., Cardich, J. and Dale, A.W. (2016) Depletion of oxygen, nitrate and nitrite in the Peruvian oxygen minimum zone cause an imbalance of benthic nitrogen fluxes. Deep-Sea Res Pt I 112, 113-122.
Stookey, L.L. (1970) Ferrozine - a New Spectrophotometric Reagent for Iron. Anal Chem 42, 779-&.
Thamdrup, B., Dalsgaard, T. and Revsbech, N.P. (2012) Widespread functional anoxia in the oxygen minimum zone of the Eastern South Pacific. Deep-Sea Res Pt I 65, 36-45.
Thunell, R., Pride, C., Tappa, E. and Mullerkarger, F. (1993) Varve Formation in the Gulf-of-California - Insights from Time-Series Sediment Trap Sampling and Remote-Sensing. Quaternary Sci Rev 12, 451-&.
Thunell, R.C. (1998) Seasonal and annual variability in particle fluxes in the Gulf of California: A response to climate forcing. Deep-Sea Res Pt I 45, 2059-2083.
Thunell, R.C., Pride, C.J., Tappa, E. and Mullerkarger, F.E. (1994) Biogenic Silica Fluxes and Accumulation Rates in the Gulf of California. Geology 22, 303-306.
Tossell, J.A. (2005) Calculating the partitioning of the isotopes of Mo between oxidic and sulfidic species in aqueous solution. Geochim Cosmochim Ac 69, A210-A210.
Trefry, J.H., Butterfield, D.B., Metz, S., Massoth, G.J., Trocine, R.P. and Feely, R.A. (1994) Trace-Metals in Hydrothermal Solutions from Cleft Segment on the Southern Juan-De-Fuca Ridge. J Geophys Res-Sol Ea 99, 4925-4935.
Tribovillard, N., Riboulleau, A., Lyons, T. and Baudin, F.O. (2004) Enhanced trapping of molybdenum by sulfurized marine organic matter of marine origin in Mesozoic limestones and shales. Chem Geol 213, 385-401.
Ulloa, O., Canfield, D.E., DeLong, E.F., Letelier, R.M. and Stewart, F.J. (2012) Microbial oceanography of anoxic oxygen minimum zones. P Natl Acad Sci USA 109, 15996-16003.
Urey, H.C. (1947) The Thermodynamic Properties of Isotopic Substances. J Chem Soc, 562-581.
Voegelin, A.R., Nagler, T.F., Samankassou, E. and Villa, I.M. (2009) Molybdenum isotopic composition of modern and Carboniferous carbonates. Chem Geol 265, 488-498.
von Damm, K.L., Edmond, J.M., Measures, C.I. and Grant, B. (1985) Chemistry of Submarine Hydrothermal Solutions at Guaymas Basin, Gulf of California. Geochim Cosmochim Ac 49, 2221-2237.
Vorlicek, T.P. and Helz, G.R. (2002) Catalysis by mineral surfaces: Implications for Mo geochemistry in anoxic environments. Geochim Cosmochim Ac 66, 3679-3692.
Wagner, M., Chappaz, A. and Lyons, T.W. (2017) Molybdenum speciation and burial pathway in weakly sulfidic environments: Insights from XAFS. Geochim Cosmochim Ac 206, 18-29.
Wasylenki, L.E., Rolfe, B.A., Weeks, C.L., Spiro, T.G. and Anbar, A.D. (2008) Experimental investigation of the effects of temperature and ionic strength on Mo isotope fractionation during adsorption to manganese oxides. Geochim Cosmochim Ac 72, 5997-6005.
Wasylenki, L.E., Weeks, C.L., Bargar, J.R., Spiro, T.G., Hein, J.R. and Anbar, A.D. (2011) The molecular mechanism of Mo isotope fractionation during adsorption to birnessite. Geochim Cosmochim Ac 75, 5019-5031.
Willbold, M. and Elliott, T. (2017) Molybdenum isotope variations in magmatic rocks. Chem Geol 449, 253-268.
Wille, M., Kramers, J.D., Nagler, T.F., Beukes, N.J., Schroder, S., Meisel, T., Lacassie, J.P. and Voegelin, A.R. (2007) Evidence for a gradual rise of oxygen between 2.6 and 2.5 Ga from Mo isotopes and Re-PGE signatures in shales. Geochim Cosmochim Ac 71, 2417-2435.
Wyrtki, K. (1962) The Oxygen Minima in Relation to Ocean Circulation. Deep-Sea Research 9, 11-23.

Zehr, J.P. (2009) New twist on nitrogen cycling in oceanic oxygen minimum zones. P Natl Acad Sci USA 106, 4575-4576.
Zheng, Y., Anderson, R.F., van Geen, A. and Kuwabara, J. (2000) Authigenic molybdenum formation in marine sediments: A link to pore water sulfide in the Santa Barbara Basin. Geochim Cosmochim Ac 64, 4165-4178.
Zierenberg, R.A., Koski, R.A., Morton, J.L., Bowse, R.M. and Shanks, W.C. (1994) Genesis of Massive Sulfide Deposits on a Sediment-Covered Spreading Center, Escanaba Trough, Southern Gorda Ridge (Vol 88, Pg 2073, 1993). Econ Geol Bull Soc 89, 1214-1214.

**Figures**

Figure 1: Overview of the Mo isotope redox proxy prevailing under different environmental conditions with typical isotopic ranges in different redox environments (after Poulson-Brucker et al. (2009), Poulson-Brucker et al. (2012), and Siebert et al. (2003)). Black bar of "Anoxic OMZ sediments" reflects the range of Mo isotope data collected along anoxic open ocean sinks, which show an average $\delta^{98}$Mo signature of about +1.6 ‰ (grey box).

Figure 2: Schematic overview of the Guaymas Basin in the Gulf of California, sample locations and depositional settings. a) Bathymetry of the Guaymas Basin and sampling locations along cross sections. b) Cross section along the slope and location of MUC9 inside the OMZ ("OMZ core"). c) Section along the graben and hydrothermal vent field with weakly oxic bottom water and location of MUC3 ("Graben core") and MUC16 ("Vent-related core").

Figure 3: Geochemical profiles of the solid phase and pore waters obtained from sediment cores of the Guaymas Basin (Gulf of California). The first column shows concentrations of dissolved Mn, Fe and $H_2S$ in the pore water. The second column shows Mn/Al ratios (dashed line indicates the Mn/Al ratio of the continental background (UCC)) as well as the degree of pyritization ($Fe_{Py}/Fe_{HR}$). Mn, Al, $Fe_{Py}$, and $Fe_{HR}$ concentrations are all given in wt-%. The third and fourth columns show the Mo content and $\delta^{98}$Mo of the pore water as well as $Mo_{auth}$ content $\delta^{98}Mo_{auth}$ of the solid phase, respectively. The Mo content and $\delta^{98}$Mo of the average continental background (UCC) and of the global seawater are shown as solid grey lines. Redox conditions (manganous, ferruginous, sulfidic) are indicated by color-coded boxes on the right side.

Figure 4: a) Cross plot of Mo isotope compositions in pore water ($\delta^{98}Mo_{PW}$) and authigenic Mo in the solid phase ($\delta^{98}Mo_{auth}$) in MUC 9 (OMZ core), MUC 3 (graben core) and MUC 16 (vent-related core). b) Cross plot of authigenic Mo and Zn in the solid phase of MUC16. c) Cross plot of authigenic Mo and its isotopic composition in the solid phase of samples from the Guaymas Basin (this study) and from the Peruvian margin OMZ and corresponding sample depth (Scholz et al. 2017). Solid black line shows the $\delta^{98}Mo$ of global seawater.

Figure 5: Simplified model of supply mechanisms of Mo into OMZ settings of the Peruvian shelf and the Guaymas slope (this study). Inserted boxes show a schematic pore water profile of aqueous Mo and the respective geochemical processes. The black arrow indicates the dissolved Mo concentration of seawater (~110 nM). a) High organic matter flux to the sediment and shallow depth of the OMZ along the Peruvian shelf induce active redox cycling in the shelf environment. Continuous Fe oxide dissolution, re-oxidation and precipitation above the sediment-water interface represent an effective Mo shuttle from the bottom water to the sediment. Due to bacterial sulfate reduction, Mo is scavenged by hydrogen sulfide from the pore water and incorporated into sulfides. This effective mechanism of Mo fixation and burial leads to high Mo mass accumulation rates. b) In the Guaymas Basin, the organic matter flux is lower and most of the exported organic material is remineralised before deposition at the seafloor within the deeper OMZ. Because of the steep slope topography, Fe oxides are transported downslope rather than repeatedly recycled between the sediments and the bottom water at the same site. Therefore, particulate Mo supply is less pronounced compared to the Peruvian shelf and Mo diffusion from bottom water plays an important role, which results in a lower Mo mass accumulation rate.

Figure 6: Concentration cross plots of a) authigenic Mo ($Mo_{auth}$) vs. total organic carbon (TOC), b) total sulfur (TS) vs. TOC and c) $Mo_{auth}$ vs. TS (data of Peru margin sediments from Scholz et al. (2017)).

Figure 7: Revised overview of the Mo isotope redox proxy. The Mo supply mechanisms are an important factor for the finally deposited isotope composition, which is demonstrated by opposing $\delta^{98}Mo$ trends in the Gulf of California (this study) and at the Peruvian margin (Scholz et al., 2017).

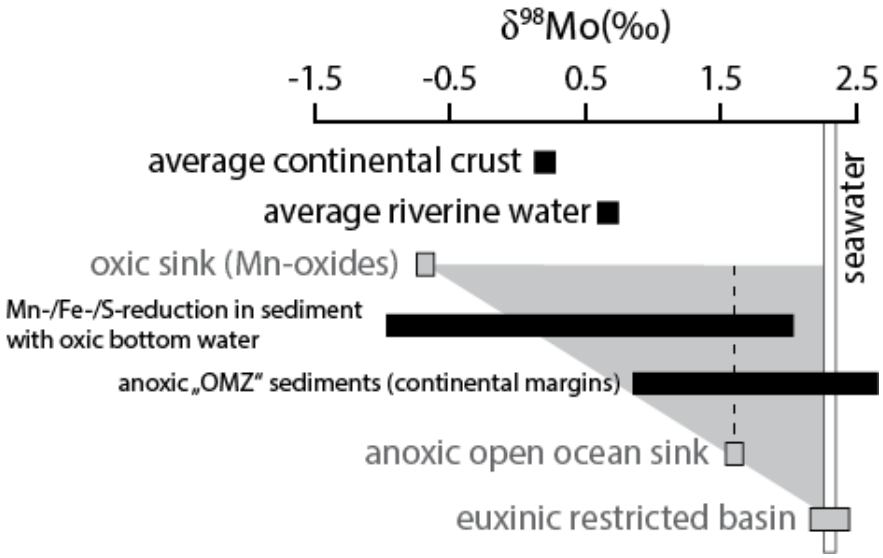


961

962 **Figure 1**

963

964

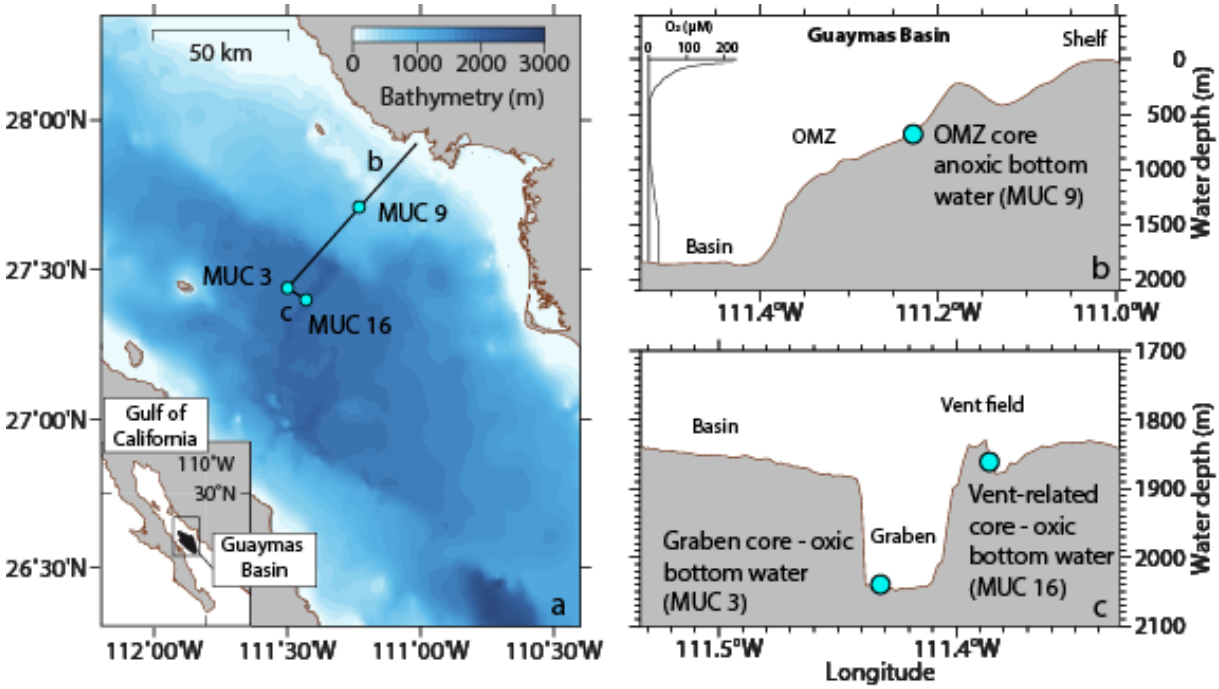


965

966 **Figure 2**

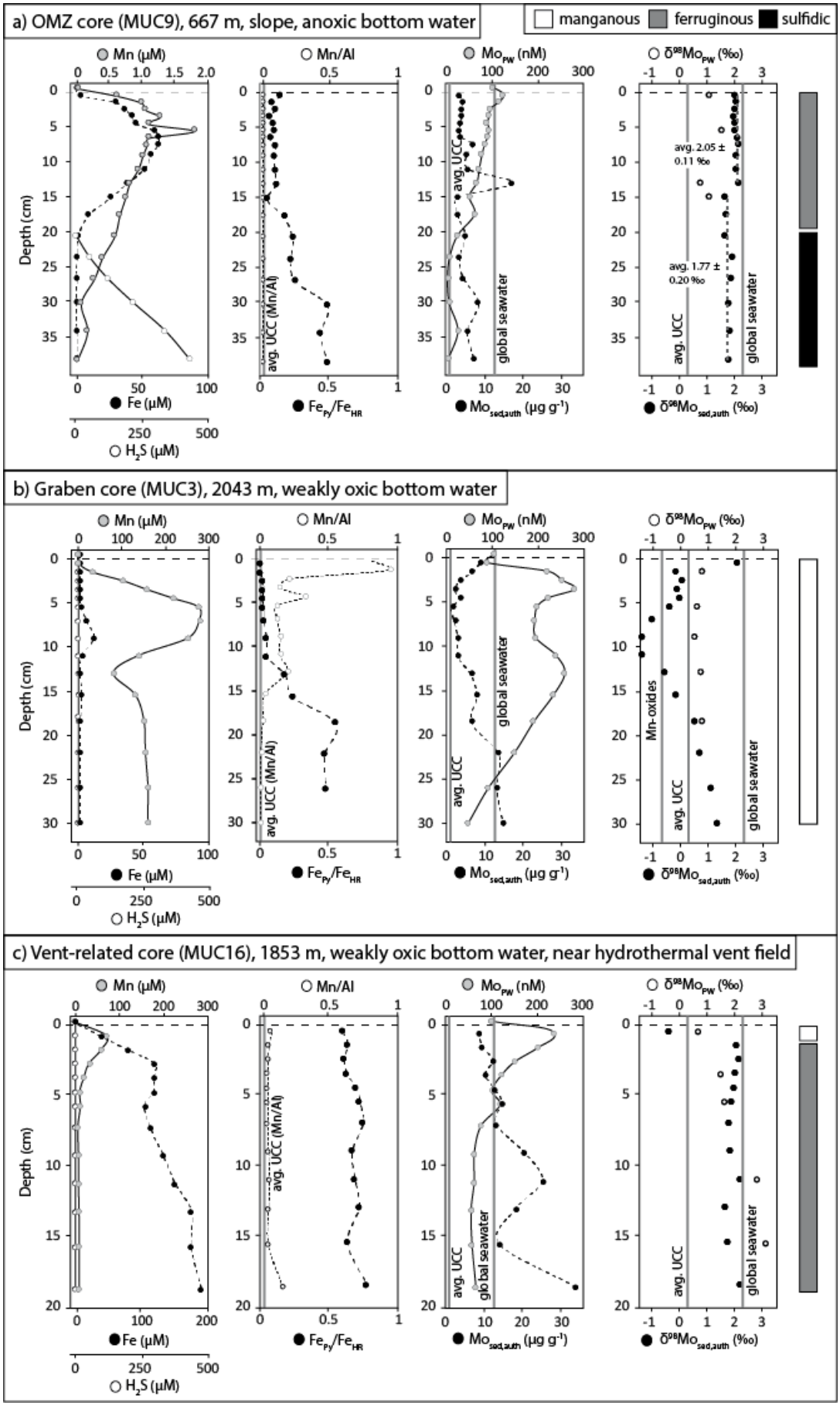


967

968 **Figure 3**

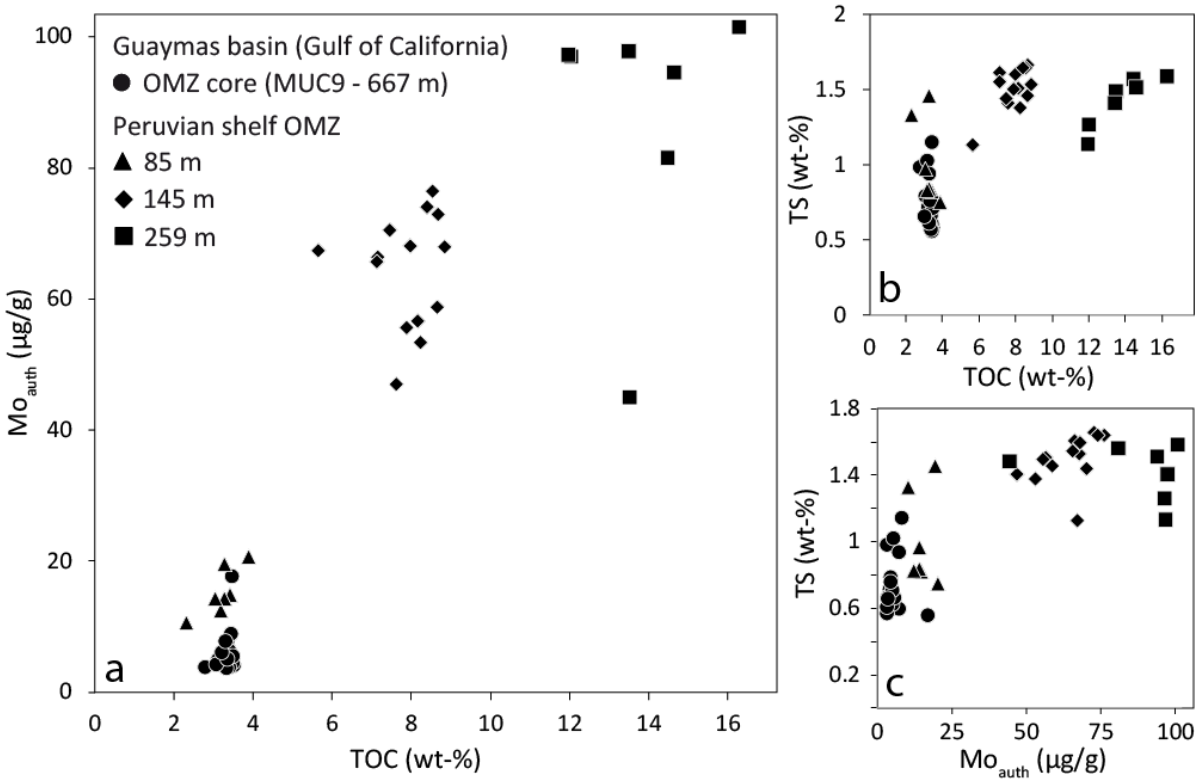
Guaymas basin (Gulf of California)
OMZ core (MUC9 - 667 m)
Peruvian shelf OMZ
85 m
145 m
259 m
Mo$_{auth}$ (µg/g)
TOC (wt-%)
a
TS (wt-%)
b
c
Mo$_{auth}$ (µg/g)

**Figure 4**

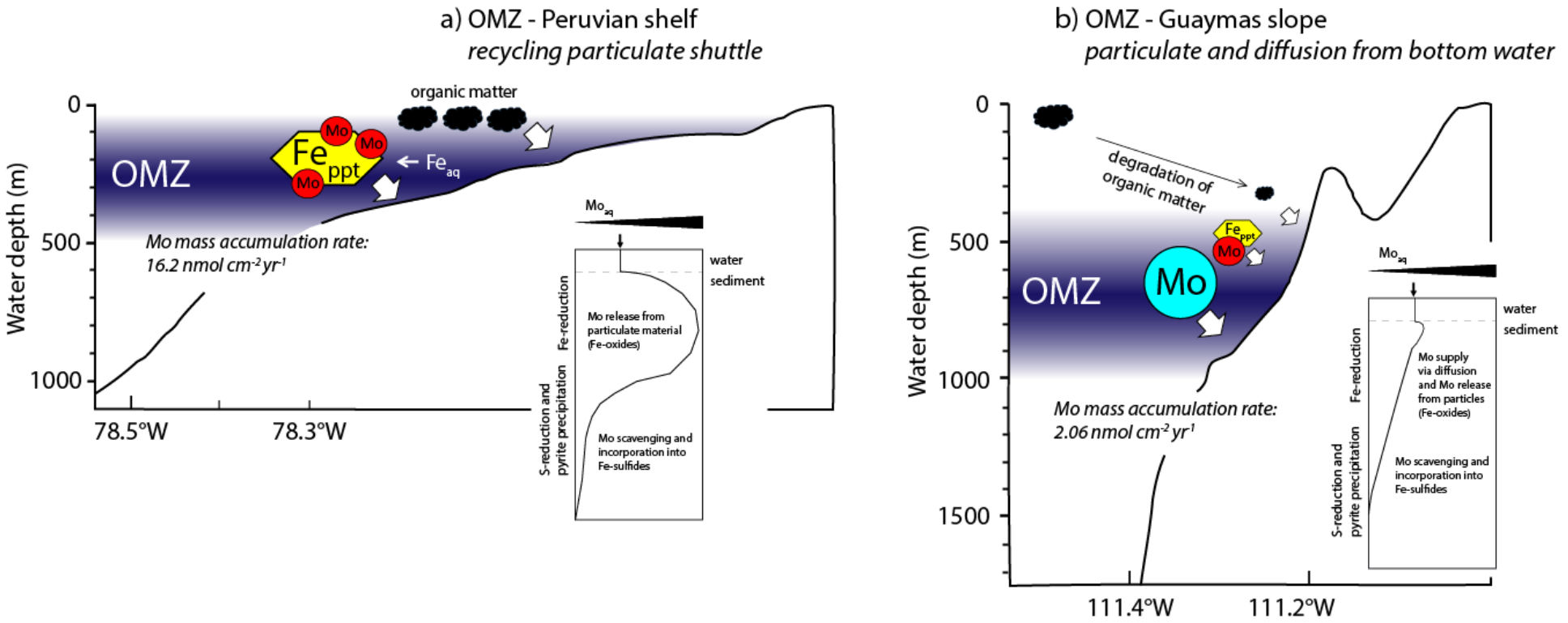


971

972 **Figure 5**

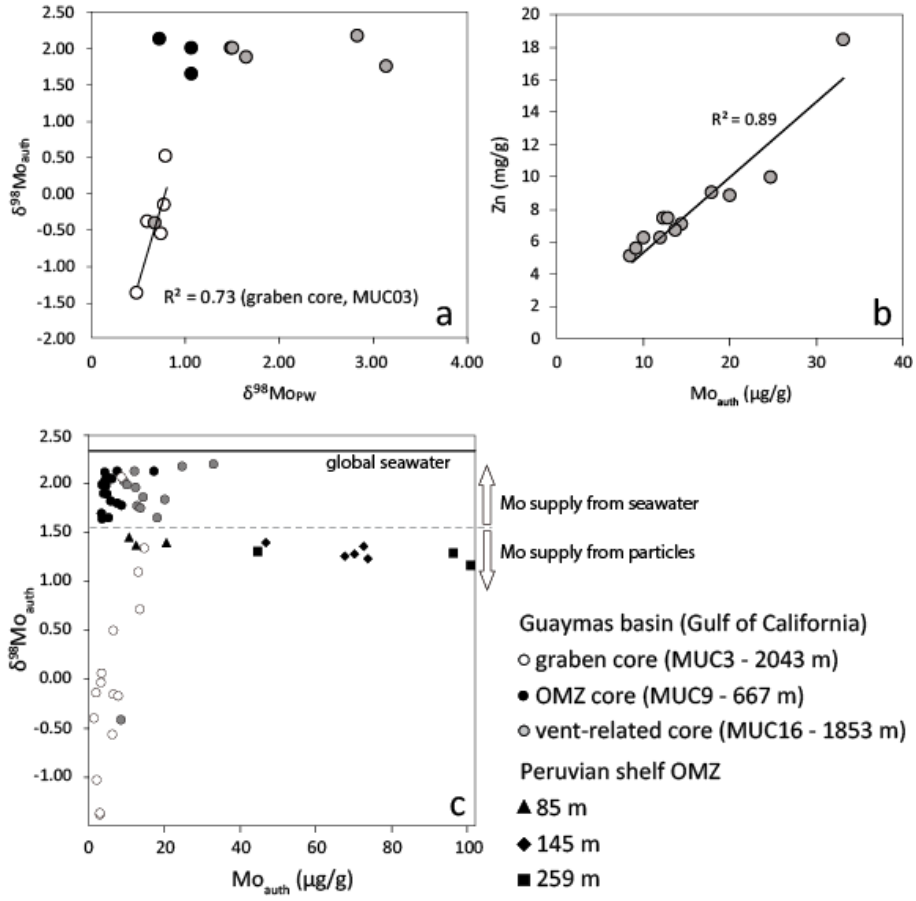


973

974 **Figure 6**

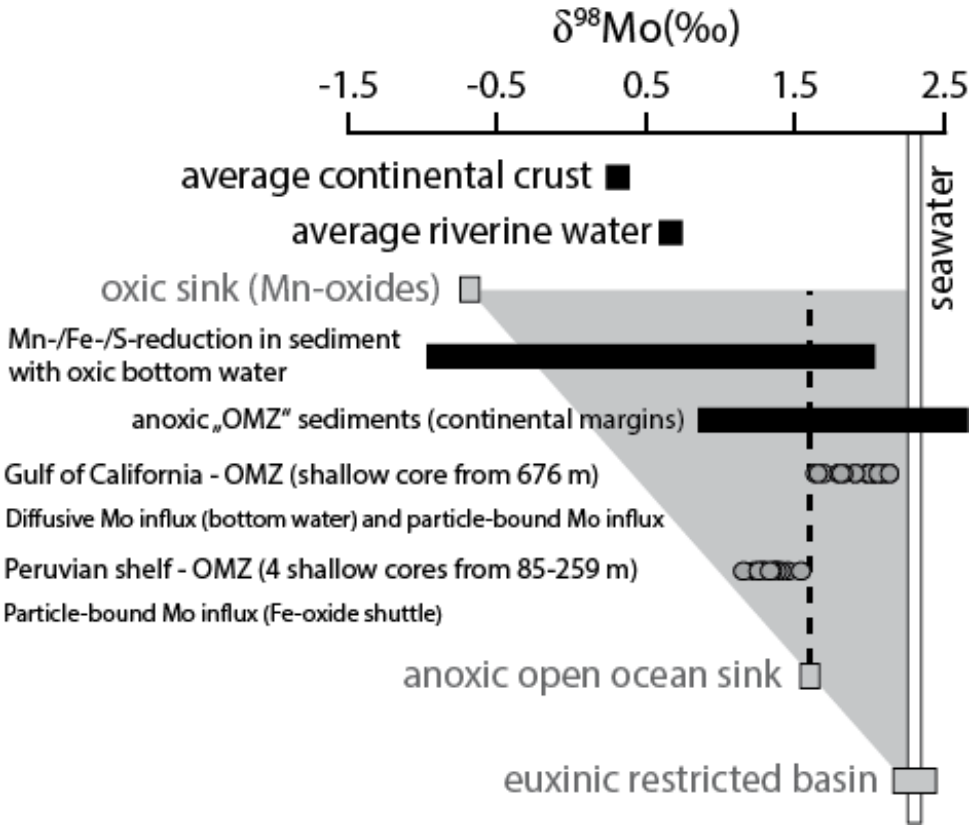


975

976 **Figure 7**

**Table 1** Location and water depth of sediment sampling stations

| Station # | Code | Device | Coordinates | Water depth [m] | Remarks |
|---|---|---|---|---|---|
| 29 | MUC9 | Multiple Corer | 27° 42.410' N<br>111° 13.656' W | 667 | "OMZ core"<br>< 2 µM $O_2$ in BW<br>TOC: 3.32 ± 0.35 (2SD) wt-% |
| 16 | MUC3 | Multiple Corer | 27° 23.827' N<br>111° 25.923' W | 2043 | "Graben core"<br>(~37 µM $O_2$ in BW)<br>TOC: 2.89 ± 0.98 (2SD) wt-% |
| 66 | MUC16 | Multiple Corer | 27° 24.577' N<br>111° 23.265' W | 1853 | "Vent-related core"<br>(~25 µM $O_2$ in BW)<br>TOC: 1.69 ± 1.18 (2SD) wt-% |

977

**Table 2** Elemental and Mo isotope composition of sediment and porewater profiles of MUC9

| | Solid phase | | | | | | | | | Porewater | | | | |
|---|---|---|---|---|---|---|---|---|---|---|---|---|---|---|
| Sediment depth [cm] | Al [wt-%] | Mn [wt-%] | Fe [wt-%] | $Fe_{Py}/Fe_{HR}$ [wt-%] | Mo [µg/g] | $Mo_{auth}$ [µg/g] | $\delta^{98}Mo$ [‰] | $\delta^{98}Mo_{auth}$ [‰] | TOC [wt-%] | Mn [µM] | Fe [µM] | $H_2S$ [µM] | Mo [nM] | $\delta^{98}Mo$ [‰] |
| bottom water | | | | | | | | | | 0.050 | 0.418 | | 106 | |
| 0 - 1 | 3.51 | 0.02 | 1.73 | 0.15 | 4.13 | 3.49 | 1.73 | 1.99 | 2.79 | 0.630 | 2.807 | | 130 | 1.07 |
| 1 - 2 | 4.66 | 0.02 | 2.24 | 0.09 | 5.37 | 4.53 | 1.79 | 2.07 | 3.12 | 1.008 | 29.99 | | 121 | |
| 2 - 3 | 4.89 | 0.02 | 2.28 | 0.11 | 5.05 | 4.16 | 1.73 | 2.03 | 3.25 | 1.076 | 36.64 | | 101 | |
| 3 - 4 | 4.72 | 0.02 | 2.27 | 0.08 | 5.24 | 4.38 | 1.70 | 1.98 | 3.24 | 1.296 | 41.68 | | 99 | |
| 4 - 5 | 4.86 | 0.02 | 2.33 | 0.09 | 4.70 | 3.81 | 1.68 | 2.00 | 3.37 | 1.124 | 45.03 | | 94 | |
| 5 - 6 | 5.11 | 0.03 | 2.43 | 0.11 | 4.68 | 3.75 | 1.66 | 2.00 | 3.52 | 1.829 | 59.15 | *below detection limit* | 98 | 1.50 |
| 6 - 7 | 5.04 | 0.02 | 2.38 | 0.08 | 5.00 | 4.09 | 1.78 | 2.12 | 3.50 | 1.120 | 61.9 | | 95 | |
| 7 - 8 | 5.34 | 0.03 | 2.50 | 0.12 | 8.32 | 7.35 | 1.91 | 2.13 | 3.37 | 1.096 | 61.4 | | 88 | |
| 8 - 10 | 5.18 | 0.02 | 2.39 | 0.11 | 6.37 | 5.43 | 1.79 | 2.05 | 3.31 | 1.033 | 56.49 | | 82 | |
| 10 - 12 | 3.95 | 0.02 | 1.66 | 0.11 | 6.69 | 5.97 | 1.86 | 2.05 | 3.40 | 0.958 | 51.04 | | 76 | |
| 12 - 14 | 4.86 | 0.02 | 2.20 | 0.12 | 18.11 | 17.23 | 2.04 | 2.13 | 3.48 | 0.827 | 38.25 | | 70 | 0.74 |
| 14 - 16 | 5.33 | 0.02 | 2.42 | 0.05 | 4.37 | 3.40 | 1.34 | 1.64 | 3.40 | 0.763 | 26.05 | | 54 | 1.07 |
| 16 - 19 | 5.38 | 0.02 | 2.45 | 0.18 | 4.25 | 3.27 | 1.37 | 1.69 | 3.33 | 0.675 | 9.088 | | 65 | |
| 19 - 22 | 5.33 | 0.02 | 2.46 | 0.24 | 6.10 | 5.13 | 1.44 | 1.65 | 3.52 | 0.593 | 1.478 | 4 | 27 | |
| 22 - 25 | 5.61 | 0.03 | 2.53 | 0.23 | 4.77 | 3.75 | 1.56 | 1.90 | 3.09 | 0.406 | 0.469 | 54 | 10 | |
| 25 - 28 | 4.78 | 0.02 | 2.16 | 0.26 | 5.59 | 4.72 | 1.65 | 1.90 | 3.37 | 0.281 | 0.424 | 120 | 5 | |
| 28 - 32 | 4.15 | 0.02 | 2.13 | 0.50 | 9.30 | 8.54 | 1.66 | 1.78 | 3.46 | 0.076 | 0.332 | 218 | 9 | |
| 32 - 36 | 4.59 | 0.02 | 2.14 | 0.45 | 6.60 | 5.76 | 1.63 | 1.82 | 3.22 | 0.170 | 0.378 | 338 | 28 | |
| 36 - 40 | 4.58 | 0.02 | 2.02 | 0.50 | 8.22 | 7.38 | 1.65 | 1.80 | 3.33 | 0.025 | 0.378 | 430 | 7 | |

$Fe_{HR}$ and $Fe_{Py}$ measured via Fe speciation; $Fe_{HR}$ is the sum of $Fe_{carb}$, $Fe_{ox1}$, $Fe_{ox2}$, $Fe_{mag}$, and $Fe_{Py}$

978

**Table 3** Elemental and Mo isotope composition of sediment and porewater profiles of MUC3

| | Solid phase | | | | | | | | | Porewater | | | | |
|---|---|---|---|---|---|---|---|---|---|---|---|---|---|---|
| Sediment depth [cm] | Al [wt-%] | Mn [wt-%] | Fe [wt-%] | $Fe_{Py}/Fe_{HR}$ [wt-%] | Mo [µg/g] | $Mo_{auth}$ [µg/g] | $\delta^{98}Mo$ [‰] | $\delta^{98}Mo_{auth}$ [‰] | TOC [wt-%] | Mn [µM] | Fe [µM] | $H_2S$ [µM] | Mo [nM] | $\delta^{98}Mo$ [‰] |
| bottom water | | | | | | | | | | 0.530 | 0.206 | | 106 | |
| 0 - 1 | 3.56 | 2.99 | 1.83 | 0.03 | 9.24 | 8.59 | 1.94 | 2.07 | 2.35 | 0.639 | 0.148 | | 88 | |
| 1 - 2 | 3.61 | 3.48 | 1.85 | 0.03 | 7.06 | 6.40 | -0.12 | -0.16 | 3.11 | 32 | 0.148 | | 222 | 0.79 |
| 2 - 3 | 3.61 | 0.81 | 1.81 | 0.05 | 4.01 | 3.35 | 0.10 | 0.06 | 3.30 | 103 | 0.148 | | 253 | |
| 3 - 4 | 3.54 | 0.54 | 1.82 | 0.05 | 2.55 | 1.91 | -0.03 | -0.14 | 3.18 | 160 | 0.194 | | 282 | |
| 4 - 5 | 2.57 | 0.88 | 1.41 | 0.05 | 3.73 | 3.26 | 0.00 | -0.04 | 3.20 | 220 | 0.286 | | 224 | |
| 5 - 6 | 3.60 | 0.49 | 1.82 | 0.05 | 1.89 | 1.23 | -0.16 | -0.41 | 3.34 | 279 | 0.928 | | 199 | 0.61 |
| 6 - 8 | 3.57 | 0.50 | 1.80 | 0.05 | 2.63 | 1.98 | -0.70 | -1.03 | 3.24 | 281 | 4.458 | *below detection limit* | 193 | |
| 8 - 10 | 3.50 | 0.56 | 1.76 | 0.07 | 3.49 | 2.86 | -1.08 | -1.39 | 3.28 | 255 | 10.28 | | 195 | 0.50 |
| 10 - 12 | 3.62 | 0.57 | 1.82 | 0.08 | 3.53 | 2.88 | -1.06 | -1.37 | 3.19 | 140 | 1.478 | | 239 | |
| 12 - 14 | 3.19 | 0.67 | 1.65 | 0.20 | 6.83 | 6.25 | -0.50 | -0.57 | 2.84 | 81 | 0.286 | | 259 | 0.75 |
| 14 - 17 | 2.39 | 0.11 | 1.15 | 0.26 | 8.22 | 7.78 | -0.15 | -0.18 | 2.16 | 132 | 1.065 | | 234 | |
| 17 - 20 | 1.87 | 0.06 | 0.80 | 0.57 | 6.83 | 6.49 | 0.49 | 0.50 | 1.67 | 152 | 0.469 | | 191 | 0.80 |
| 20 - 24 | 2.87 | 0.06 | 1.39 | 0.49 | 14.05 | 13.53 | 0.70 | 0.71 | 2.74 | 156 | 0.194 | | 149 | |
| 24 - 28 | 2.91 | 0.05 | 1.40 | 0.50 | 13.60 | 13.07 | 1.06 | 1.09 | 2.80 | 161 | 0.194 | | 92 | |
| 28 - 32 | 3.03 | 0.05 | 1.47 | --- | 15.28 | 14.73 | 1.30 | 1.34 | 2.92 | 161 | 0.148 | | 47 | |

$Fe_{HR}$ and $Fe_{Py}$ measured via Fe speciation; $Fe_{HR}$ is the sum of $Fe_{carb}$, $Fe_{ox1}$, $Fe_{ox2}$, $Fe_{mag}$, and $Fe_{Py}$

979

**Table 4** Elemental and Mo isotope composition of sediment and porewater profiles of MUC16

| | Solid phase | | | | | | | | | Porewater | | | | |
|---|---|---|---|---|---|---|---|---|---|---|---|---|---|---|
| Sediment depth [cm] | Al [wt-%] | Mn [wt-%] | Fe [wt-%] | $Fe_{Py}/Fe_{HR}$ [wt-%] | Mo [µg/g] | $Mo_{auth}$ [µg/g] | $\delta^{98}Mo$ [‰] | $\delta^{98}Mo_{auth}$ [‰] | Zn [µg/g] | Mn [µM] | Fe [µM] | $H_2S$ [µM] | Mo [nM] | $\delta^{98}Mo$ [‰] |
| bottom water | | | | | | | | | | 0.196 | 0.441 | | 102 | |
| 0 - 1 | 1.79 | 0.09 | 24.49 | 0.61 | 8.92 | 8.60 | -0.39 | -0.42 | 5037 | 79 | 40 | | 241 | 0.69 |
| 1 - 2 | 1.93 | 0.06 | 24.44 | 0.64 | 9.64 | 9.29 | 1.97 | 2.03 | 5507 | 67 | 81 | | 204 | |
| 2 - 3 | 1.80 | 0.05 | 29.79 | 0.62 | 12.39 | 12.06 | 2.08 | 2.13 | 6158 | 37 | 122 | | 154 | |
| 3 - 4 | 1.67 | 0.04 | 21.36 | 0.64 | 10.48 | 10.17 | 1.94 | 1.99 | 6182 | 25 | 122 | | 123 | 1.52 |
| 4 - 5 | 1.58 | 0.04 | 21.59 | 0.70 | 12.68 | 12.39 | 1.93 | 1.96 | 7408 | 15 | 122 | *below detection limit* | 103 | |
| 5 - 6 | 1.55 | 0.04 | 22.14 | 0.73 | 14.73 | 14.45 | 1.83 | 1.86 | 7034 | 17 | 108 | | 121 | 1.65 |
| 6 - 8 | 1.52 | 0.04 | 22.72 | 0.76 | 13.15 | 12.87 | 1.74 | 1.77 | 7405 | 11 | 116 | | 79 | |
| 8 - 10 | 1.34 | 0.04 | 23.74 | 0.68 | 20.38 | 20.13 | 1.82 | 1.84 | 8783 | 12 | 135 | | 64 | |
| 10 - 12 | 0.94 | 0.03 | 25.98 | 0.70 | 25.00 | 24.83 | 2.16 | 2.18 | 9889 | 12 | 153 | | 64 | 2.84 |
| 12 - 14 | 1.82 | 0.05 | 22.21 | 0.73 | 18.43 | 18.10 | 1.63 | 1.65 | 8977 | 13 | 177 | | 57 | |
| 14 - 17 | 2.20 | 0.06 | 17.69 | 0.64 | 14.15 | 13.75 | 1.71 | 1.75 | 6634 | 14 | 177 | | 60 | 3.15 |
| 17 - 20 | 0.27 | 0.04 | 27.70 | 0.79 | 33.21 | 33.17 | 2.20 | 2.20 | 18383 | 13 | 192 | | 68 | |

$Fe_{HR}$ and $Fe_{Py}$ measured via Fe speciation; $Fe_{HR}$ is the sum of $Fe_{carb}$, $Fe_{ox1}$, $Fe_{ox2}$, $Fe_{mag}$, and $Fe_{Py}$

980

**Table 5** Comparison of geochemical parameters in the Guaymas OMZ and the Peruvian margin OMZ

| Parameter | Guaymas OMZ | Peruvian margin OMZ |
|---|---|---|
| OMZ (m water depth) | 500 - 1000 [a] | < 50 - 500 [b] |
| OMZ position | slope | shelf |
| Primary production (g C m-2 yr-1) | 130 [c] | 350 [d] |
| TOC content (wt-%) | 2.79 - 3.52 | 2.31 - 16.10 [b] |
| Sedimentary processes | · Negligible release of Fe at sediment-water interface<br>· Moderate bacterial sulfide reduction | · Recycling of Fe-oxide dissolution/ re-oxidation and precipitation at sediment-water interface<br>· Enhanced bacterial sulfide reduction and precipitation of Fe-sulfides |
| Mo flux (nmol cm-2 yr-1) | 2.06 | 16.2 [b] |
| Mo content (porewater in nM) | 5 - 130 (avg. of 92 nM before Fe-S precipitation) | 12-218 (avg. of 153 nM before Fe-S precipitation) |
| Mo content (sediment in µg/g) | 3 - 17 | 11 - 101 [b] |
| avg. $\delta^{98}$Mo (sediment in ‰) | 1.93 ± 0.32 (2SD) | 1.32 ± 0.17 (2SD) [e] |
| Mo supply mechanism | diffusive and particulate | particulate (Fe-oxides) [e] |

[a] Bray, 1988; Thunell, 1998; Wyrtki, 1962

[b] Scholz et al., 2011

[c] Brumsack, 1989

[d] Muller and Suess, 1979

[e] Scholz et al., 2017

981